
Test-Time Adaptation of Vision-Language Models for Open-Vocabulary Semantic Segmentation

Mehrdad Noori* David Osowiechi* Gustavo A. Vargas Hakim Ali Bahri
 Moslem Yazdanpanah Sahar Dastani Farzad Beizaee Ismail Ben Ayed
 Christian Desrosiers

LIVIA, ÉTS Montréal, Canada
 International Laboratory on Learning Systems (ILLIS)

Abstract

Recently, test-time adaptation has attracted wide interest in the context of vision-language models for image classification. However, to the best of our knowledge, the problem is completely overlooked in dense prediction tasks such as Open-Vocabulary Semantic Segmentation (OVSS). In response, we propose a novel TTA method tailored to adapting VLMs for segmentation during test time. Unlike TTA methods for image classification, our Multi-Level and Multi-Prompt (MLMP) entropy minimization integrates features from intermediate vision-encoder layers and is performed with different text-prompt templates at both the global CLS token and local pixel-wise levels. Our approach could be used as plug-and-play for any segmentation network, does not require additional training data or labels, and remains effective even with a single test sample. Furthermore, we introduce a comprehensive OVSS TTA benchmark suite, which integrates a rigorous evaluation protocol, seven segmentation datasets, and 15 common corruptions, **with a total of 82 distinct test scenarios**, establishing a standardized and comprehensive testbed for future TTA research in open-vocabulary segmentation. Our experiments on this suite demonstrate that our segmentation-tailored method consistently delivers significant gains over direct adoption of TTA classification baselines. Our code can be found at [our repository](#).

1 Introduction

Contrastive Vision-Language Models (VLMs) such as CLIP [1] have demonstrated remarkable generalization capabilities by aligning vision and language modalities through large-scale pre-training. This versatility has positioned VLMs as powerful foundation models for numerous downstream tasks [2, 3, 4]. A promising direction for leveraging VLMs beyond classification is Open-Vocabulary Semantic Segmentation (OVSS), where models aim to segment objects beyond a pre-defined set of categories, via VLMs’ zero-shot recognition capabilities. Unlike traditional segmentation methods that require pixel-wise supervision, OVSS enables generalization to unseen object categories through language-driven representations.

Although existing OVSS methods have made significant progress, they remain vulnerable to domain shifts at test time, such as environmental changes or image corruptions, which may dramatically degrade segmentation quality. In the absence of a mechanism enabling to adapt to unseen test-time distributions, these models might lose their generalization capabilities, which limits their reliability in real-world applications. Consequently, there is an unresolved gap for the Test-Time Adaptation (TTA) of OVSS models, which would enable models to dynamically adjust both to the task shift of VLM-based segmentation and to the domain shifts encountered during inference.

*Equal contribution

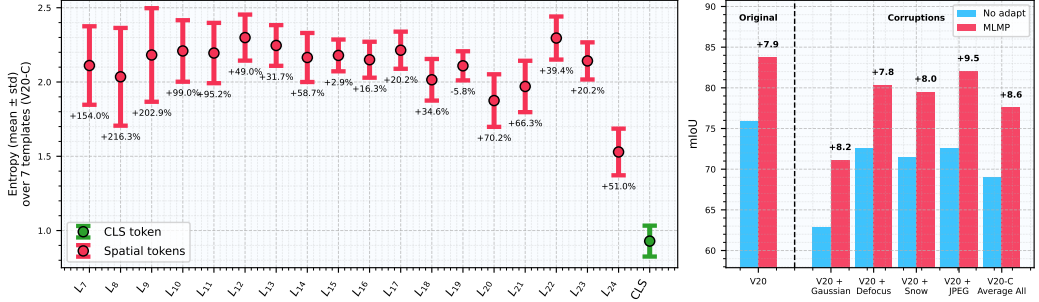


Figure 1: **Motivation.** (a) **Left:** Mean \pm std entropy across seven text templates for the CLS token and the spatial tokens of the final and intermediate vision layers. Even the final-layer spatial tokens exhibit higher entropy and variability than CLS, and this sensitivity grows further in intermediate layers (numbers show % std increase relative to CLS). These patterns highlight pronounced prompt-induced uncertainty at multiple depths and motivate both multi-level and multi-prompt adaptation. (b) **Right:** mIoU of the baseline vs MLMP on clean and corrupted data, showing consistent absolute improvements and underscoring the effectiveness of our joint adaptation strategies.

To close this gap, we present a novel **Multi-Level Multi-Prompt** (MLMP) test time adaptation strategy, the first fully test-time adaptation framework that could be plugged into *any OVSS model*, to the best of our knowledge. MLMP is lightweight and plug-and-play, boosting performance on the fly without access to labels. Its power comes from two key ideas: (i) adaptively integrating intermediate vision-encoder layers to harvest complementary, shift-resilient features, and (ii) a multi-prompt optimization that exploits VLMs’ template sensitivity to provide a robust adaptation signal across diverse text-template conditions.

The core requirement for test-time adaptation is a reliable signal that faithfully reflects the current input distribution—even under severe domain shifts or corruptions. To meet this need, MLMP begins by adaptively integrating intermediate layers of the vision encoder: earlier layers preserve fine-grained edges and textures, while deeper blocks encode semantic context, and each layer reacts differently when the data distribution changes. By aggregating these multi-level features into the adaptation process and weighting them by their confidence, MLMP harvests the most trustworthy signals for each input sample.

Beyond multi-level fusion, MLMP leverages VLMs’ prompt sensitivity to model uncertainty. Prior work [5, 6] shows that changing a prompt template, e.g., from ‘a photo of a {class}’ to ‘an origami of a {class}’, could drastically change the classification performance. *In segmentation, we show that this effect is even more extreme: per-pixel predictions under different prompts diverge far more than the single CLS token used for classification (Fig. 1a: CLS token vs. last-layer spatial tokens). This sensitivity effect is even more pronounced in intermediate feature maps. The intermediate layers that we fuse for reliability exhibit even stronger template-specific shifts (Fig. 1a: intermediate-layer tokens).* Instead of viewing this inconsistency as a weakness, MLMP models it directly by incorporating multi-prompt, multi-level predictions into its adaptation objective function. This multi-prompt approach not only smooths out template-specific noise, thereby reducing gradient variance and preventing degenerate collapse, but also ensures that the model yields segmentations that are consistent across diverse linguistic formulations. In this way, MLMP transforms prompt sensitivity into a powerful adaptation signal that complements its multi-level feature integration. As illustrated in Fig. 1b, our MLMP method consistently outperforms the non-adapted baseline, achieving about 8–9 absolute mIoU improvements on domain-shifted inputs, while also boosting performance on original (non-corrupted) images. This demonstrates the benefit of our joint multi-level, multi-prompt adaptation.

We outline our key contributions as follows:

- **Plug-and-Play TTA Framework for OVSS:** We introduce MLMP, which is, to the best of our knowledge, the first fully test-time adaptation method that could be easily applied to any OVSS backbone.
- **Adaptive Multi-Level Fusion:** MLMP integrates features from intermediate vision-encoder layers to capture complementary, shift-resilient cues. To further enhance robustness, we propose

an uncertainty-aware strategy that re-weights features from individual layers based on their prediction entropy.

- **Multi-Prompt Local-Global Test Time Optimization:** MLMP turns prompt sensitivity into signal by directly minimizing entropy across different text prompt templates at both the global CLS token and local pixel-wise levels. This optimization naturally complements our multi-layer feature fusion by enforcing consistency across linguistic perspectives and feature depths.
- **Comprehensive OVSS TTA Benchmark Suite:** We curate a rigorous evaluation protocol spanning seven mainstream segmentation datasets and 15 common corruptions, **with a total of 82 distinct test scenarios**, establishing a standardized and comprehensive testbed for future TTA research in open-vocabulary segmentation. Our experiments on this suite demonstrate that MLMP consistently delivers significant gains over baselines across all scenarios.

2 Related Work

Test-time adaptation (TTA) for open-vocabulary semantic segmentation (OVSS) remains unexplored—existing TTA methods focus on classification or single-modal segmentation, while OVSS approaches use VLMs without any online adaptation. We bridge this gap with our proposed method MLMP, a plug-and-play TTA framework that could be applied to any OVSS method.

Test-Time Adaptation. TTA addresses domain shifts by adapting pre-trained models to unlabeled target data without source samples. Methods like PTBN [7] and TENT [8] update batch statistics and affine parameters via entropy minimization but rely on large batches or augmentations. MEMO [9] simplifies this with single-sample augmentations, LAME [10] clusters features via Laplacian smoothing, and SAR [11] stabilizes adaptation using batch-agnostic normalization and sharpness-aware entropy minimization.

Test-Time Adaptation on Segmentation. TTA enhances segmentation robustness against domain shifts without source data. Methods include self-supervised adaptation via entropy minimization or contrastive learning [8, 12], single-image adaptation optimizing per-image predictions [13], and continual TTA that leverages clustering to prevent forgetting [14]. Multi-modal adaptation uses cross-modal self-supervision [15], while active TTA integrates minimal human feedback for guided refinement [16]. These approaches assume a fixed, vision-only label space and rely on spatial or surrogate tasks, making them ill-suited for zero-shot, text-driven OVSS. Consequently, none have been applied to VLMs.

Open-Vocabulary Semantic Segmentation. OVSS enables segmentation of unseen categories using vision-language models like CLIP. Approaches fall into fully-supervised, weakly-supervised, and training-free categories. Fully-supervised methods use pixel-wise annotations [17, 18, 19], while weakly-supervised ones leverage image-text pairs [20, 21, 22, 23]. Training-free OVSS avoids adaptation data but may rely on auxiliary pre-trained models [24, 25, 26]. Training-free OVSS approaches aim to enhance segmentation without additional training data. Some methods, such as SCLIP [27], adjust self-attention mechanisms to improve feature localization, while others, like MaskCLIP [28], refine feature extraction from CLIP’s visual backbone. GEM [29] introduces additional optimization techniques to extract better dense features without fine-tuning. Among these, NACLIP [30] enhances CLIP’s dense prediction capabilities by introducing neighborhood attention, which ensures that image patches focus on nearby regions, and by refining similarity measures to improve spatial consistency.

To the best of our knowledge, this is the first work to address TTA for OVSS models, filling a previously unexplored intersection between these fields.

3 Methodology

We first revisit the contrastive vision–language model (VLM) for open-vocabulary semantic segmentation (OVSS), and then present our Multi-Level Multi-Prompt (MLMP) adaptation strategy.

3.1 OVSS with VLMs

Given an input image $\mathbf{X} \in \mathbb{R}^{H \times W \times 3}$ and a set of concepts $C_k \in \mathcal{C}$ expressed in natural language, OVSS seeks a semantic mask $\mathbf{y} \in \{1, \dots, K\}^{H \times W}$ that assigns one concept to every pixel.

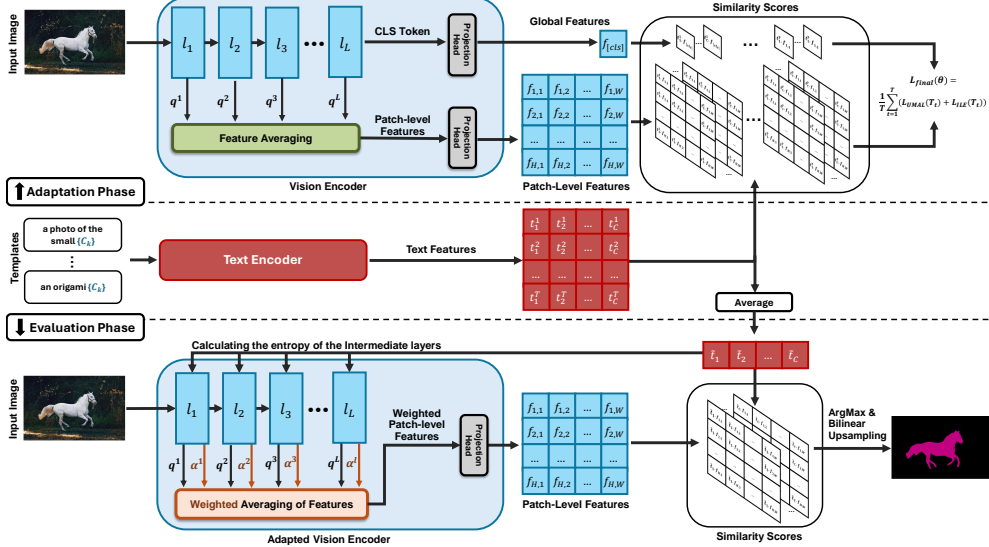


Figure 2: Overview of our MLMP method. In the Adaptation Phase, the model is adapted by leveraging multiple prompt templates alongside various intermediate feature layers, as well as the global feature. During the Evaluation Phase, the model computes weights based on the entropy of the intermediate features to perform a weighted averaging. These averaged features, combined with the different templates, are then used to generate the final segmentation map.

Following recent approaches for OVSS [30, 27], we employ a transformer-based VLM to extract visual and text features from the image and concepts in natural language. Specifically, we feed the image \mathbf{X} into the ViT-based vision encoder to extract a visual token matrix $\mathbf{F} = [\mathbf{f}_{[\text{cls}]}, \mathbf{f}_1, \dots, \mathbf{f}_N]$ with each $\mathbf{f}_i \in \mathbb{R}^D$, where $N = \lfloor H/s \rfloor \times \lfloor W/s \rfloor$ is the number of patches of size $s \times s$ in the image and $[\text{cls}]$ is the CLS token for classification. We define $\mathbf{Q} = [\mathbf{q}_{[\text{cls}]}, \mathbf{q}_1, \dots, \mathbf{q}_N]$, with each $\mathbf{q}_i \in \mathbb{R}^{D'}$, the output features before the projection layer: $\mathbf{F} = \text{proj}(\mathbf{Q})$. At the same time, the text encoder is employed to extract text features $\mathbf{t}_k \in \mathbb{R}^D$ for each concept $C_k \in \mathcal{C}$. This is achieved by combining C_k with a text prompt template, for instance “A photo of a $[C_k]$ ” or “An image of a $[C_k]$ ” where C_k is an arbitrary text description like “white horse”.

The standard approach for classifying images with a contrastive VLM such as CLIP [1] computes the cosine between the CLS token features and text embeddings of classes, and assigns the image to the class with highest similarity:

$$\arg \max_k \text{sim}(\mathbf{f}_{[\text{cls}]}, \mathbf{t}_k), \text{ where } \text{sim}(\mathbf{x}, \mathbf{y}) = \frac{\mathbf{x} \cdot \mathbf{y}}{\|\mathbf{x}\| \|\mathbf{y}\|}. \quad (1)$$

For extending this approach to segmentation, we instead compute the similarity between *patch* embeddings \mathbf{f}_i and text embeddings \mathbf{t}_k and assign a class/concept to each patch.

3.2 MLMP: Proposed Method

Figure 2 illustrates our full test-time adaptation pipeline, **MLMP**. MLMP integrates three complementary ideas: **uncertainty-aware multi-level fusion**, **image-level entropy minimization** and **multi-prompt adaptation**.

We begin by modifying the entropy minimization objective of TENT [8] from image classification to work with *spatial tokens*. More specifically, for a batch of B images, each containing N tokens, the probability that token i belongs to concept k is

$$p_{ik} = \frac{\exp(\text{sim}(\mathbf{f}_i, \mathbf{t}_k)/\tau)}{\sum_{k'=1}^{|C|} \exp(\text{sim}(\mathbf{f}_i, \mathbf{t}_{k'})/\tau)}. \quad (2)$$

where τ is a softmax temperature scaling parameter, $\mathbf{T} = [\mathbf{t}_1, \dots, \mathbf{t}_{|C|}]$, and $\text{norm}(\cdot)$ denotes a function normalizing the columns of its input matrix to unit length. Also, let \mathbf{P} denote a matrix

containing the probabilities in (2), which could be expressed more compactly as follows:

$$\mathbf{P} = \text{softmax}(\text{norm}(\mathbf{F}) \cdot \text{norm}(\mathbf{T})^\top / \tau). \quad (3)$$

The batch-wise entropy, which is minimized for adaptation, is then defined as follows:

$$\mathcal{H}(\mathbf{P}) = -\frac{1}{B \cdot N} \sum_{i=1}^{B \cdot N} \sum_{k=1}^{|\mathcal{C}|} p_{ik} \log p_{ik}. \quad (4)$$

Following [5, 31], we keep the entire text encoder frozen and update only the *LayerNorm* parameters of the vision encoder during adaptation. Freezing the text encoder greatly reduces computational overhead, since text embeddings can be precomputed and reused across all test samples.

Uncertainty-Aware Multi-Level Fusion. In VLM-based classification, the CLS token in the last layer of the visual encoder is typically used to compute the class label probabilities. This approach relies on the idea that the relevant information for classification lies at the end of the ViT and that intermediate layers serve to transform features. In segmentation, however, features from intermediate layers are often used to capture complementary information at different scales [32]. This hypothesis is validated in Fig. 1b, and more specifically in Table 1), showing that a higher segmentation mIoU is obtained when combining the features from different layers near the end of the ViT.

Inspired by this result, and leveraging the useful property of ViTs that the output of each layer has the same shape, we extend the entropy-based loss described above to use features from *multiple layers*. Denoting as \mathbf{q}_i^ℓ the visual features of patch i obtained at layer ℓ , we seek to aggregate the multi-level features into a single vector $\bar{\mathbf{q}}_i$ for segmentation prediction. A simple approach for doing this is to compute $\bar{\mathbf{q}}_i$ by averaging \mathbf{q}_i^ℓ across all layers ℓ . However, this approach ignores the relative contribution and confidence of each layer in the final segmentation. To address this limitation, we estimate a confidence weight α^ℓ for each layer ℓ based on its prediction entropy. First, we get visual features $\mathbf{F}_i^\ell = \text{proj}(\mathbf{Q}_i^\ell)$ using the *same* projection head as for the final segmentation. Following the same approach as before, we then compute the batch-wise entropy of layer ℓ as

$$h^\ell = \mathcal{H}(\mathbf{P}^\ell), \quad \text{with } \mathbf{P}^\ell = \text{softmax}(\text{norm}(\mathbf{F}^\ell) \cdot \text{norm}(\mathbf{T})^\top / \tau). \quad (5)$$

Finally, the confidence weight of the layer is obtained using a softmax as follows:

$$\alpha^\ell = \frac{\exp(-\beta \cdot h^\ell)}{\sum_{\ell'=1}^L \exp(-\beta \cdot h^{\ell'})}. \quad (6)$$

Here, β is a parameter controlling the “sharpness” of the weight distribution. During adaptation, we set $\beta = 0$ to promote a uniform contribution from all layers in the prediction. During inference, we sharpen the distribution with a value of $\beta = 1$, emphasizing the more confident layers in the final prediction.

With these confidence weights, we can now obtain our uncertainty-aware multi-level (UAML) features as

$$\bar{\mathbf{F}} = \text{proj}(\bar{\mathbf{Q}}), \quad \text{with } \bar{\mathbf{Q}} = \sum_{\ell=1}^L \alpha^\ell \mathbf{Q}^\ell, \quad (7)$$

giving the following entropy-based loss to minimize:

$$\mathcal{L}_{\text{UAML}}(\mathbf{T}) = \mathcal{H}(\bar{\mathbf{P}}), \quad \text{with } \bar{\mathbf{P}} = \text{softmax}(\text{norm}(\bar{\mathbf{F}}) \cdot \text{norm}(\mathbf{T})^\top / \tau). \quad (8)$$

Image-Level Entropy Minimization. Since the CLS token is not directly linked to individual patch predictions but rather captures a more global representation of the input, we also include an image-level entropy (ILE) minimization term specifically for this token. As illustrated in Fig. 1, the CLS token demonstrates increased robustness and reliability. This term, which encourages the model to produce more confident global predictions is expressed as:

$$\mathcal{L}_{\text{ILE}}(\mathbf{T}) = -\frac{1}{B} \sum_{b=1}^B \sum_{k=1}^{|\mathcal{C}|} p_{b,k}^{[\text{cls}]} \log p_{b,k}^{[\text{cls}]} . \quad (9)$$

Here, $p_{b,k}^{[\text{cls}]}$ denotes the predicted probability for concept C_k obtained using the CLS token in the last layer for the b -th sample.

Multi-Prompt Adaptation. Prior work on TTA for classification [5] has shown the usefulness of leveraging multiple prompt templates in VLM to encode class labels, based on the idea that the templates capture complementary information about these classes. As shown in Fig. 1a, the sensitivity to the choice of prompt templates is even more pronounced in segmentation tasks, where fine-grained spatial predictions are required. Using multiple templates acts as cross-modal regularization, encouraging more stable and generalized learning signals. While different from image augmentation, it can be seen as a strong, safe, and lightweight text-space augmentation. Rather than averaging the weights adapted from different prompt templates as in [5]—a computationally expensive approach for dense prediction tasks such as segmentation—our method minimizes our proposed UAML and ILE losses across these templates. Let \mathbf{T}_t be the text features obtained using the t -th template. Our final adaptation loss is defined as:

$$\mathcal{L}_{\text{final}}(\theta) = \frac{1}{T} \sum_{t=1}^T (\mathcal{L}_{\text{UAML}}(\mathbf{T}_t) + \mathcal{L}_{\text{ILE}}(\mathbf{T}_t)). \quad (10)$$

Theoretical Justification. Each template t contributes its own adaptation loss, as we optimize their average in Eq. (10). By optimizing the adaptation loss of each prompt directly, we force the model to correct for the unique wording and visual cue of each template, rather than ‘averaging’ these differences in the text embedding space. This loss-level integration treats each template as an independent critic, translating diverse linguistic perspectives into separate gradient signals. Averaging those signals produces an unbiased descent direction whose variance decays as $1/T$, enabling each adaptation step to represent the full prompt ensemble while being stable under noisy shifts.

Proposition 1 (Unbiasedness and Variance Bound). Assume that each per-template gradient $g_t(\theta) = \nabla_{\theta} [\mathcal{L}_{\text{UAML}}(\mathbf{T}_t) + \mathcal{L}_{\text{ILE}}(\mathbf{T}_t)]$ has variance bounded by σ^2 , then the ensemble gradient, defined by $\nabla_{\theta} \mathcal{L}_{\text{final}} = \frac{1}{T} \sum_{t=1}^T g_t(\theta)$, is unbiased and satisfies the following variance bound:

$$\mathbb{E}[\nabla_{\theta} \mathcal{L}_{\text{final}}] = \mathbb{E}[g_t(\theta)]; \quad \text{Var}(\nabla_{\theta} \mathcal{L}_{\text{final}}) = \frac{1}{T^2} \sum_{t=1}^T \text{Var}(g_t(\theta)) \leq \frac{\sigma^2}{T} \quad (11)$$

Proof. A proof of Prop. 1 is provided in Appendix A. \square

The $1/T$ reduction in gradient variance, as stated in Prop. 1, explains the improved stability we observe. Table 3 confirms that this loss-level ensemble outperforms alternative fusion strategies.

4 Experimental Settings

Experimental Setup. Following prior work on TTA in classification [31, 5], we restrict updates to the normalization layers within the vision encoder. The adaptation process is carried out over 10 iterations using the Adam optimizer with a constant learning rate of 10^{-3} across all datasets. We use a batch size of 2 images during adaptation across all datasets. For each new batch, the model undergoes a reset, restoring it to its initial weights before adaptation is applied.

Datasets. In traditional TTA for segmentation, two datasets are commonly employed to simulate domain shifts—one for model training and another for adaptation during inference (e.g., GTAV and Cityscapes)—as both must share the same semantic label space. In our study, as this is the first exploration of TTA for VLMs in segmentation tasks and given that VLMs are pre-trained, we draw inspiration from ImageNet-C [33] to introduce 15 synthetic corruptions on segmentation datasets. Our experiments are conducted on Pascal VOC 20 (v20), Pascal VOC 21 (v21) [34], Pascal Context 59 (P59), Pascal Context 60 (P60) [35], and Cityscapes [36], incorporating both original version (clean) and the synthetic 15 corruptions (denoted with a “-C” suffix). For COCO-Stuff [37] and COCO-Object [38], we use only the original versions. This setup results in 82 distinct test scenarios covering both synthetic and realistic domain shifts, with variations in resolution, scene diversity, object sizes, and class granularity—enabling a comprehensive evaluation of our method’s robustness.

Benchmarking. While MLMP is compatible with any OVSS framework, we incorporate NA-CLIP [30] with ViT-L/14 as our baseline OVSS model, which leverages neighborhood attention to enhance spatial consistency in a training-free manner. The compared methods include TENT [8], which serves as a baseline and minimizes entropy during adaptation; CLIPArTT [31], which employs

Table 1: mIoU performance when using different layer ranges in the proposed multi-level adaptation.

ViT-L/14 Layer Range	L_{24} (last)	L_{23-24} (last two)	L_{22-24} (last three)	L_{19-24} (last 25%)	L_{13-24} (last 50%)	L_{7-24} (last 75%)	L_{1-24} (all layers)
V20 (Original)	77.00 ± 0.04	77.65 ± 0.02	77.66 ± 0.09	80.61 ± 0.05	80.50 ± 0.03	81.67 ± 0.04	78.79 ± 0.02
Gaussian Noise	63.02 ± 0.06	64.41 ± 0.05	65.39 ± 0.13	66.88 ± 0.18	66.88 ± 0.02	67.82 ± 0.01	63.06 ± 0.09
Defocus Blur	72.06 ± 0.12	72.93 ± 0.19	72.84 ± 0.02	76.10 ± 0.16	76.37 ± 0.05	78.78 ± 0.02	77.56 ± 0.09
Snow	71.04 ± 0.05	72.09 ± 0.04	72.56 ± 0.02	74.47 ± 0.12	74.41 ± 0.01	76.39 ± 0.02	73.72 ± 0.07
JPEG Compression	71.84 ± 0.15	73.88 ± 0.11	74.40 ± 0.07	76.96 ± 0.02	77.67 ± 0.03	78.73 ± 0.08	75.87 ± 0.19
V20-C Average	69.33	70.33	70.78	72.89	73.45	74.90	72.02

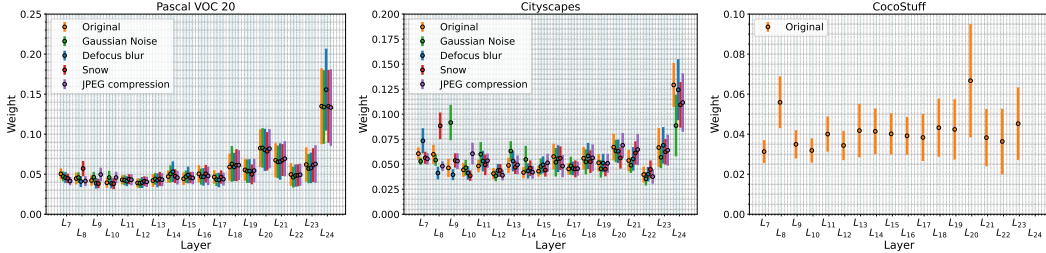


Figure 3: Mean and standard deviation of layer-wise confidence weights of MLMP across datasets. The fusion mechanism adaptively emphasizes more reliable layers based on input conditions.

pseudo-labels generated via conformal learning; WATT [5], which averages learnable parameters across multiple parallel branches; and TPT [6], which performs prompt tuning to adapt VLMs at test time. For a fair comparison, we modified all methods for the segmentation setting by processing all spatial tokens extracted from the VLM, rather than relying solely on the CLS token.

5 Results

5.1 Ablation studies

Effect of Intermediate Layers. To analyze the impact of layer selection in our uncertainty-aware multi-level adaptation strategy, we use different ranges of intermediate layers. As shown in Table 1, performance varies notably with the fusion range. While using only the final layers yields moderate improvements, incorporating the last 75% of the layers consistently achieves the best performance across both clean and corrupted inputs. This highlights that multi-level fusion is a key driver of adaptation performance: earlier layers, although less semantically abstract, contribute valuable low-level features—such as texture and edge cues—that enhance robustness to distribution shifts. In this ablation, we isolate the effect of multi-level fusion by applying only the first term in Eq. 10, using a single prompt template and omitting the L_{ILE} term.

Effect of Uncertainty-Aware Layer Fusion. We investigate strategies for aggregating multi-level features by comparing uniform averaging ($\beta = 0$) and uncertainty-aware fusion ($\beta = 1$) during evaluation, using the same 75% layer range identified in the previous ablation. As shown in Table 2, incorporating entropy-based weighting improves performance by 4.29% on V20 and 3.31% on V20-C. This highlights the importance of leveraging layer-wise confidence when aggregating features.

Visualization of Layer-Wise Confidence Weights. We visualize the mean and standard deviation of the learned layer weights to better understand the behavior of our uncertainty-aware fusion strategy. As shown in Fig. 3, deeper layers tend to receive higher confidence, though earlier layers also contribute, especially under corrupted conditions. This variation is most pronounced in the Cityscapes dataset, where the distribution fluctuates more across layers and corruption types. In contrast, the COCO-Stuff dataset shows a flatter distribution, where the final layer is not consistently the most influential. These results underscore the core strength of our fusion mechanism: its ability to adaptively reweight layers based on input conditions, assigning greater importance to those that remain more reliable under distribution shifts and corruption. Please refer to Appendix H for additional results on other datasets.

Effect of Global Image-Level Adaptation Term. The image-level entropy term, L_{ILE} complements our patch-level adaptation by encouraging consistent global predictions through the CLS token. While the multi-level loss targets fine-grained spatial predictions, the ILE term introduces global context that

Table 2: mIoU comparison of MLMP components, showing individual and combined contributions.

Multi-Level Fusion	x	✓	✓	x	x	✓	✓	✓	x	✓	✓
Multi-Prompt Loss	x	x	x	✓	x	✓	✓	x	x	✓	✓
Image-Level Entropy	x	x	x	x	✓	x	x	✓	✓	✓	✓
Uncertainty-Aware Weighting	x	x	✓	x	x	x	✓	x	x	x	✓
V20 (Original)	77.00	77.38	81.67	79.70	78.74	78.97	83.00	77.69	82.70	81.15	79.13 83.76
Gaussian Noise	63.02	65.42	67.82	66.75	65.66	65.96	69.13	66.17	69.00	69.62	67.35 71.13
Defocus Blur	72.06	76.65	78.78	74.31	75.00	76.46	78.78	77.29	79.78	77.14	77.79 80.36
Snow	71.04	72.64	76.39	74.66	74.16	73.25	77.31	74.05	78.50	77.20	74.94 79.53
JPEG Compression	71.84	74.38	78.73	75.56	74.77	76.77	80.81	74.61	79.79	77.98	77.94 82.06
V20-C	69.33	71.59	74.90	72.58	71.99	72.66	75.97	72.41	76.18	75.08	73.89 77.58

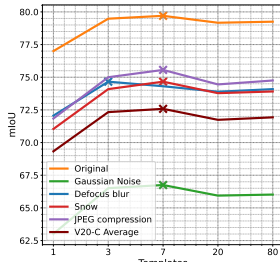


Figure 4: mIoU performance of our method for different numbers of templates.

Table 3: mIoU performance for prompt-integration strategies (Text, Params, Loss) on clean and corrupted data.

Dataset: V20	Text	Params	Loss
Original	78.91 ± 0.07	74.46 ± 0.21	79.70 ± 0.06
Gaussian Noise	66.27 ± 0.00	62.83 ± 0.04	66.75 ± 0.01
Defocus Blur	74.05 ± 0.10	70.28 ± 0.16	74.31 ± 0.09
Snow	73.78 ± 0.02	70.10 ± 0.30	74.66 ± 0.01
JPEG Compression	74.98 ± 0.05	70.55 ± 0.11	75.56 ± 0.02
V20-C Average	71.92	68.44	72.58

helps stabilize adaptation. As shown in Table 2, when added in isolation, L_{ILE} improves performance by 1.74% and 2.66% on V20 and V20-C, respectively, demonstrating the benefit of incorporating global context under distribution shift.

Effect of Number of Prompt Templates. To isolate this effect, we evaluate performance using different numbers of prompt templates while disabling both the multi-level fusion and the image-level entropy (ILE) term in Eq.10. As shown in Fig.4, increasing the number of templates improves performance up to 7, after which the gains begin to saturate or slightly decline. This trend holds across both clean and corrupted settings, indicating that a moderate number of diverse prompt templates is sufficient for MLMP. We therefore use 7 templates by default in our main experiments. Please refer to Appendix C for template details.

Where to Integrate Multi-Prompt Information. Here, we empirically compare strategies for integrating multi-prompt information into the adaptation process. Specifically, we evaluate: (1) text-level averaging, where prompt embeddings are averaged before computing logits—a technique commonly used in zero-shot learning [1]; (2) a learnable parameter averaging baseline (Params) inspired by WATT [5]; and (3) our proposed method (Loss), which incorporates all prompt templates directly into the adaptation loss (Eq.10). To isolate the effect of prompt integration, this analysis excludes other components such as multi-level fusion and the image-level entropy (ILE) term. As shown in Table 3, our loss-level formulation consistently outperforms the alternatives across both clean and corrupted settings.

Full Component Analysis. Table 2 presents an extensive ablation evaluating the contribution of each component in our MLMP strategy. Each proposed element yields consistent gains when added independently, but it is their combination that delivers the highest overall performance across both clean and corrupted settings, highlighting their strong complementary effects within a unified framework. Additionally, we provide further ablations in the Appendix, including **alternative OVSS backbones, a different VLM, ViT architecture variants, computational complexity analysis, and MLMP segmentation map visualizations**.

5.2 Final Comparison with Alternative Adaptation Methods

Performance on Clean Data (No Distributional Shift). We begin by evaluating MLMP on clean test data (original), where no distributional shift is present. This setting is crucial, as TTA methods must avoid degrading performance when adaptation is unnecessary. As shown in Table 4, MLMP achieves strong mIoU gains of +7.85, +5.66, +3.72, and +3.04 on V20, V21, P59, and P60, and +5.04/+2.91 on challenging datasets COCOObject and COCOSTuff. In contrast, most alternative

Table 4: mIoU comparison of MLMP and baselines across several datasets. CLIPArTT could not be run for a few cases owing to GPU memory shortages. Full per-dataset results are in Appendix J.

OVSS Backbone: NAACLIP		Adaptation Method				
Dataset	No Adapt.	TENT	TPT	WATT	CLIPArTT	MLMP
V20 (Original)	75.91	77.00 \pm 0.04	75.93 \pm 0.01	57.73 \pm 0.06	72.77 \pm 0.14	83.76 \pm 0.00
V20-C	Gaussian Noise	62.89	63.02 \pm 0.06	62.98 \pm 0.01	36.44 \pm 0.04	53.36 \pm 0.25
	Shot noise	66.26	65.88 \pm 0.06	66.33 \pm 0.02	40.95 \pm 0.05	58.15 \pm 0.28
	Impulse Noise	63.16	64.17 \pm 0.04	63.12 \pm 0.01	34.90 \pm 0.06	54.83 \pm 0.03
	Defocus blur	72.59	72.06 \pm 0.12	72.55 \pm 0.02	52.43 \pm 0.03	65.39 \pm 0.45
	Glass blur	71.44	70.74 \pm 0.07	71.40 \pm 0.01	49.96 \pm 0.05	64.62 \pm 0.13
	Motion blur	73.10	73.50 \pm 0.10	73.16 \pm 0.02	53.35 \pm 0.06	67.48 \pm 0.17
	Zoom blur	59.03	61.36 \pm 0.07	59.00 \pm 0.01	41.39 \pm 0.08	52.37 \pm 0.12
	Snow	71.49	71.04 \pm 0.05	71.44 \pm 0.01	51.18 \pm 0.06	66.97 \pm 0.02
	Frost	65.38	67.01 \pm 0.02	65.46 \pm 0.01	45.75 \pm 0.05	60.48 \pm 0.08
	Fog	70.69	70.54 \pm 0.07	70.70 \pm 0.01	52.96 \pm 0.04	67.85 \pm 0.10
	Brightness	74.95	75.61 \pm 0.02	74.95 \pm 0.01	55.82 \pm 0.05	71.52 \pm 0.14
	Contrast	71.51	70.51 \pm 0.04	71.49 \pm 0.02	50.74 \pm 0.06	66.01 \pm 0.06
	Elastic transform	62.86	65.78 \pm 0.05	62.95 \pm 0.01	45.45 \pm 0.04	60.41 \pm 0.10
	Pixelate	77.28	76.95 \pm 0.12	77.31 \pm 0.01	59.76 \pm 0.05	73.14 \pm 0.17
	JPEG compression	72.59	71.84 \pm 0.15	72.56 \pm 0.01	53.44 \pm 0.05	68.21 \pm 0.07
Mean		69.01	69.33	69.03	48.30	63.39
V21 (Original)	45.12	45.65 \pm 0.02	45.17 \pm 0.01	28.58 \pm 0.05	39.50 \pm 0.04	50.78 \pm 0.02
V21-C	40.75	40.95	40.77	24.12	34.16	46.25
P59 (Original)	28.23	28.73 \pm 0.02	28.26 \pm 0.01	16.55 \pm 0.04	24.60 \pm 0.03	31.95 \pm 0.02
P59-C	23.88	23.88	23.88	13.37	19.72	27.03
P60 (Original)	24.95	25.29 \pm 0.01	24.98 \pm 0.01	14.77 \pm 0.03	21.88 \pm 0.03	27.99 \pm 0.03
P60-C	21.39	21.25	21.49	12.08	17.79	24.07
CityScapes (Original)	29.49	30.54 \pm 0.04	29.57 \pm 0.01	20.77 \pm 0.06	—	33.35 \pm 0.03
CityScapes-C	21.63	21.64	21.60	13.45	—	23.02
COCOObject (Original)	23.80	24.88 \pm 0.01	23.84 \pm 0.01	14.14 \pm 0.06	21.34 \pm 0.03	28.84 \pm 0.01
COCOStuff (Original)	18.34	18.76 \pm 0.01	18.35 \pm 0.01	9.49 \pm 0.02	15.48 \pm 0.01	21.25 \pm 0.01

adaptation methods fail to improve performance in this setting. These gains highlight the robustness and generalization of our method, even when no explicit domain shift is present.

Performance Under Distributional Shift. Under distributional shifts, the advantages of MLMP become even more apparent. As shown in Table 4, MLMP consistently outperforms both the zero-shot baseline and existing adaptation methods, achieving mIoU gains of +8.60, +5.50, +3.15, and +2.68 on V20-C, V21-C, P59-C, and P60-C, respectively. Beyond standard corruptions, we further evaluate on the Cityscapes dataset, which presents natural domain shifts such as environmental variation, weather conditions, and resolution differences. Despite its challenging nature and low zero-shot performance, MLMP improves mIoU by +3.86, demonstrating its real-world adaptability. To push this further, we apply 15 corruption types to create Cityscapes-C, where MLMP still yields a +1.39 gain. While TENT provides modest improvements, most other adaptation methods—including ClipArTT, TPT, and WATT—either fail to improve or degrade performance. These results highlight that naive strategies like pseudo-labeling, prompt tuning, or weight averaging are insufficient for open-vocabulary segmentation, and emphasize the need for segmentation-specific adaptation techniques such as MLMP. Detailed results can be found in Appendix H.

6 Conclusion

We presented MLMP, a plug-and-play test-time adaptation framework for open-vocabulary semantic segmentation that can be integrated with any OVSS method. By combining uncertainty-aware fusion of intermediate ViT features with a novel loss-level integration of multiple prompt templates, MLMP consistently enhances performance across both clean and shifted domains—including common corruptions and natural distributional shifts. Our comprehensive OVSS-TTA benchmark—covering seven datasets and 82 distinct test scenarios—demonstrates MLMP’s broad applicability and establishes a rigorous evaluation protocol for future work in adaptive, language-aware segmentation. While MLMP demonstrates strong, consistent gains, there remain opportunities to further refine its components. In particular, our current layer-weighting mechanism relies on entropy estimates from a shared projection head, which may not fully reflect each layer’s unique characteristics. Future work could investigate more flexible architectures—such as lightweight adapters or dedicated projection modules per layer—to more accurately assess and fuse intermediate features.

References

- [1] Alec Radford, Jong Wook Kim, Chris Hallacy, Aditya Ramesh, Gabriel Goh, Sandhini Agarwal, Girish Sastry, Amanda Askell, Pamela Mishkin, Jack Clark, et al. Learning transferable visual models from natural language supervision. In *International conference on machine learning*, pages 8748–8763. PMLR, 2021.
- [2] Ziyi Lin, Shijie Geng, Renrui Zhang, Peng Gao, Gerard De Melo, Xiaogang Wang, Jifeng Dai, Yu Qiao, and Hongsheng Li. Frozen clip models are efficient video learners. In *European Conference on Computer Vision*, pages 388–404. Springer, 2022.
- [3] Andrey Guzhov, Federico Raue, Jörn Hees, and Andreas Dengel. Audioclip: Extending clip to image, text and audio. In *ICASSP 2022-2022 IEEE International Conference on Acoustics, Speech and Signal Processing (ICASSP)*, pages 976–980. IEEE, 2022.
- [4] Jie Liu, Yixiao Zhang, Jie-Neng Chen, Junfei Xiao, Yongyi Lu, Bennett A Landman, Yixuan Yuan, Alan Yuille, Yucheng Tang, and Zongwei Zhou. Clip-driven universal model for organ segmentation and tumor detection. In *Proceedings of the IEEE/CVF International Conference on Computer Vision*, pages 21152–21164, 2023.
- [5] David Osowiechi, Mehrdad Noori, Gustavo Vargas Hakim, Moslem Yazdanpanah, Ali Bahri, Milad Cheraghalkhani, Sahar Dastani, Farzad Beizaee, Ismail Ayed, and Christian Desrosiers. Watt: Weight average test time adaptation of clip. In A. Globerson, L. Mackey, D. Belgrave, A. Fan, U. Paquet, J. Tomczak, and C. Zhang, editors, *Advances in Neural Information Processing Systems*, volume 37, pages 48015–48044. Curran Associates, Inc., 2024.
- [6] Manli Shu, Weili Nie, De-An Huang, Zhiding Yu, Tom Goldstein, Anima Anandkumar, and Chaowei Xiao. Test-time prompt tuning for zero-shot generalization in vision-language models. *Advances in Neural Information Processing Systems*, 35:14274–14289, 2022.
- [7] Zachary Nado, Shreyas Padhy, D. Sculley, Alexander D’Amour, Balaji Lakshminarayanan, and Jasper Snoek. Evaluating prediction-time batch normalization for robustness under covariate shift. *arXiv:2006.10963 [cs, stat]*, January 2021. arXiv: 2006.10963.
- [8] Dequan Wang, Evan Shelhamer, Shaoteng Liu, Bruno Olshausen, and Trevor Darrell. Tent: Fully test-time adaptation by entropy minimization. *arXiv preprint arXiv:2006.10726*, 2020.
- [9] Marvin Zhang, Sergey Levine, and Chelsea Finn. Memo: Test time robustness via adaptation and augmentation. *Advances in neural information processing systems*, 35:38629–38642, 2022.
- [10] Malik Boudiaf, Romain Mueller, Ismail Ben Ayed, and Luca Bertinetto. Parameter-free online test-time adaptation. In *IEEE/CVF Conference on Computer Vision and Pattern Recognition (CVPR)*, pages 8344–8353, 2022.
- [11] Shuaicheng Niu, Jiaxiang Wu, Yifan Zhang, Zhiqian Wen, Yaofo Chen, Peilin Zhao, and Mingkui Tan. Towards stable test-time adaptation in dynamic wild world, 2023.
- [12] Hong Liu, Guoliang Kang, Shan You, Jiancheng Bao, Mingkui Li, and Yao Zhang. Source-free domain adaptation for semantic segmentation. *IEEE Transactions on Pattern Analysis and Machine Intelligence*, 2021.
- [13] Jiacheng He, Zhilu Zhang, Zhen Wang, and Yan Huang. Autoencoder based test-time adaptation for semantic segmentation. In *Proceedings of the IEEE/CVF International Conference on Computer Vision (ICCV)*, pages 998–1007, 2021.
- [14] Charanpal D Mummadli, Matthias Arens, and Thomas Brox. Test-time adaptation for continual semantic segmentation. In *Proceedings of the IEEE/CVF Conference on Computer Vision and Pattern Recognition (CVPR)*, pages 11828–11837, 2021.
- [15] Gabriele Valvano, Andrea Leo, Kuniaki Saito, and Tatiana Tommasi. Learning multi-modal self-supervision for test-time adaptation. In *NeurIPS*, 2023.
- [16] Zhi Wang, Yue Zhang, Kun Yu, and Hao Zhang. Active test-time adaptation for semantic segmentation. *arXiv preprint arXiv:2312.01835*, 2023.

[17] Davide Barsellotti, Roberto Amoroso, and Barbara Caputo. Enhancing open-vocabulary semantic segmentation with prototype retrieval. In *Pattern Recognition. ICPR International Workshops and Challenges*, pages 243–258. Springer, 2023.

[18] Golnaz Ghiasi, Yin Cui, Aravind Srinivas, Rui Qian, Tsung-Yi Lin, Ekin D Cubuk, Quoc V Le, and Barret Zoph. Scaling open-vocabulary image segmentation with image-level labels. In *European Conference on Computer Vision*, pages 343–360. Springer, 2022.

[19] Feng Liang, Bichen Wu, Xiaoliang Dai, Kunpeng Li, Yinan Zhao, Hang Zhang, Peizhao Zhang, Peter Vajda, and Diana Marculescu. Open-vocabulary semantic segmentation with mask-adapted clip. In *Proceedings of the IEEE/CVF Conference on Computer Vision and Pattern Recognition*, pages 7061–7070, 2023.

[20] Kaixin Cai, Pengzhen Ren, Yi Zhu, Hang Xu, Jianzhuang Liu, Changlin Li, Guangrun Wang, and Xiaodan Liang. Mixreorg: Cross-modal mixed patch reorganization is a good mask learner for open-world semantic segmentation. In *Proceedings of the IEEE/CVF International Conference on Computer Vision*, pages 1196–1205, 2023.

[21] Junbum Cha, Jonghwan Mun, and Byungseok Roh. Learning to generate text-grounded mask for open-world semantic segmentation from only image-text pairs. In *Proceedings of the IEEE/CVF Conference on Computer Vision and Pattern Recognition*, pages 11165–11174, 2023.

[22] Yuxin Chen, Yujie Li, Zhaoxiang Zhang, and Yunchao Liu. Exploring open-vocabulary semantic segmentation from clip vision encoder distillation only. In *Proceedings of the IEEE/CVF International Conference on Computer Vision*, pages 10010–10019, 2023.

[23] Jiarui Xu, Shalini De Mello, Sifei Liu, and Xiaolong Wang. Groupvit: Semantic segmentation emerges from text supervision. In *Proceedings of the IEEE/CVF Conference on Computer Vision and Pattern Recognition*, pages 18134–18144, 2022.

[24] Davide Barsellotti, Roberto Amoroso, and Barbara Caputo. Fossil: Free open-vocabulary semantic segmentation through synthetic references retrieval. In *Proceedings of the IEEE/CVF Winter Conference on Applications of Computer Vision*, pages 1234–1243, 2024.

[25] Andrea Corradini, Federico Bianchi, Debora Nozza, and Dirk Hovy. Freeseg-diff: Training-free open-vocabulary segmentation with diffusion models. In *Proceedings of the IEEE/CVF Winter Conference on Applications of Computer Vision*, pages 567–576, 2024.

[26] Lukas Karazija, Wafaa Bousselham, Andrei Bursuc, Thiemo Alldieck, and Patrick Pérez. Diffusion models for zero-shot open-vocabulary segmentation. In *Proceedings of the IEEE/CVF International Conference on Computer Vision*, pages 1010–1020, 2023.

[27] Feng Wang, Jieru Mei, and Alan Yuille. SCLIP: Rethinking self-attention for dense vision-language inference. In *European Conference on Computer Vision*, pages 315–332. Springer, 2025.

[28] Chong Zhou, Chen Change Loy, and Bo Dai. Extract free dense labels from clip. In *European Conference on Computer Vision*, pages 288–304. Springer, 2022.

[29] Wafaa Bousselham, Andrei Bursuc, Thiemo Alldieck, and Patrick Pérez. Grounding everything: Emerging localization properties in vision-language transformers. In *Proceedings of the IEEE/CVF Conference on Computer Vision and Pattern Recognition*, pages 5678–5687, 2024.

[30] Sina Hajimiri, Ismail Ben Ayed, and Jose Dolz. Pay attention to your neighbours: Training-free open-vocabulary semantic segmentation. In *Proceedings of the IEEE/CVF Winter Conference on Applications of Computer Vision*, 2025.

[31] Gustavo Adolfo Vargas Hakim, David Osowiechi, Mehrdad Noori, Milad Cheraghalkhani, Ali Bahri, Moslem Yazdanpanah, Ismail Ben Ayed, and Christian Desrosiers. Clipartt: Light-weight adaptation of clip to new domains at test time. *arXiv preprint arXiv:2405.00754*, 2024.

[32] Olaf Ronneberger, Philipp Fischer, and Thomas Brox. U-net: Convolutional networks for biomedical image segmentation. In *Medical image computing and computer-assisted intervention–MICCAI 2015: 18th international conference, Munich, Germany, October 5–9, 2015, proceedings, part III 18*, pages 234–241. Springer, 2015.

- [33] Dan Hendrycks and Thomas Dietterich. Benchmarking neural network robustness to common corruptions and perturbations. 2019.
- [34] Mark Everingham, Luc Van Gool, Christopher K. I. Williams, John M. Winn, and Andrew Zisserman. The pascal visual object classes (voc) challenge. *Int. J. Comput. Vis.*, 88(2):303–338, 2010.
- [35] Roozbeh Mottaghi, Xianjie Chen, Xiaobai Liu, Nam-Gyu Cho, Seong-Whan Lee, Sanja Fidler, Raquel Urtasun, and Alan Yuille. The role of context for object detection and semantic segmentation in the wild. In *IEEE Conference on Computer Vision and Pattern Recognition (CVPR)*, 2014.
- [36] Marius Cordts, Mohamed Omran, Sebastian Ramos, Timo Rehfeld, Markus Enzweiler, Rodrigo Benenson, Uwe Franke, Stefan Roth, and Bernt Schiele. The cityscapes dataset for semantic urban scene understanding. In *Proc. of the IEEE Conference on Computer Vision and Pattern Recognition (CVPR)*, 2016.
- [37] Holger Caesar, Jasper R. R. Uijlings, and Vittorio Ferrari. Coco-stuff: Thing and stuff classes in context. *CoRR*, abs/1612.03716, 2016.
- [38] Tsung-Yi Lin, Michael Maire, Serge J. Belongie, Lubomir D. Bourdev, Ross B. Girshick, James Hays, Pietro Perona, Deva Ramanan, Piotr Dollár, and C. Lawrence Zitnick. Microsoft COCO: common objects in context. *CoRR*, abs/1405.0312, 2014.
- [39] Michael Tschannen, Alexey Gritsenko, Xiao Wang, Muhammad Ferjad Naeem, Ibrahim Alabdulmohsin, Nikhil Parthasarathy, Talfan Evans, Lucas Beyer, Ye Xia, Basil Mustafa, et al. Siglip 2: Multilingual vision-language encoders with improved semantic understanding, localization, and dense features. *arXiv preprint arXiv:2502.14786*, 2025.

Test-Time Adaptation of Vision-Language Models for Open-Vocabulary Semantic Segmentation - Appendix

A Proof of Proposition 1

Unbiasedness and Variance Bound Proposition 1 (Restated): Assume each per-template gradient $g_t(\theta) = \nabla_\theta [L_{\text{UAML}}(T_t) + L_{\text{ILE}}(T_t)]$ has variance bounded by σ^2 . Then, the ensemble gradient, defined by $\nabla_\theta \mathcal{L}_{\text{final}} = \frac{1}{T} \sum_{t=1}^T g_t(\theta)$, is unbiased and satisfies the following variance bound:

$$\mathbb{E}[\nabla_\theta \mathcal{L}_{\text{final}}] = \mathbb{E}[g_t(\theta)], \quad \text{Var}(\nabla_\theta \mathcal{L}_{\text{final}}) = \frac{1}{T^2} \sum_{t=1}^T \text{Var}(g_t(\theta)) \leq \frac{\sigma^2}{T}.$$

Step 1: Unbiasedness. By linearity of expectation, we have:

$$\mathbb{E}[\nabla_\theta \mathcal{L}_{\text{final}}] = \mathbb{E}\left[\frac{1}{T} \sum_{t=1}^T g_t(\theta)\right] = \frac{1}{T} \sum_{t=1}^T \mathbb{E}[g_t(\theta)] = \mathbb{E}[g_t(\theta)].$$

Hence, averaging the gradients from all T templates gives an unbiased estimate of the true gradient of the final loss.

Step 2: Variance Bound. Assuming independence with $\text{Var}(g_t) \leq \sigma^2$, we get

$$\text{Var}(\nabla_\theta \mathcal{L}_{\text{final}}) = \text{Var}\left(\frac{1}{T} \sum_{t=1}^T g_t(\theta)\right) = \frac{1}{T^2} \sum_{t=1}^T \text{Var}(g_t(\theta)) \leq \frac{T\sigma^2}{T^2} = \frac{\sigma^2}{T}$$

Thus, the variance bound holds:

$$\text{Var}(\nabla_\theta \mathcal{L}_{\text{final}}) \leq \frac{\sigma^2}{T}.$$

This completes the proof of Proposition 1.

B Implementation Details

Unless otherwise noted, all experiments utilize NACLIP [30] with ViT-L/14 as the OVSS backbone. We adapt only the LayerNorm parameters within the vision encoder, amounting to approximately 0.02% of the model’s total parameters. Our adaptation setup follows prior work in classification [5, 31], using the Adam optimizer with a fixed learning rate of 0.001 and 10 adaptation steps (iterations) across all experiments. Additionally we use batch of 2 images during adaptation. After each batch, model weights are explicitly reset to their original pre-adaptation values to ensure that each batch is adapted independently, without leveraging information from previously processed data. Following standard settings from [1], we use the default softmax temperature value of 100 in all experiments. All images are resized to 224×224 pixels. Due to the high resolution of images in the Cityscapes dataset, we split them into overlapping patches of size 224×224 pixels with an overlap of 112 pixels between patches. The segmentation predictions from these patches are aggregated to reconstruct the final, full-resolution segmentation maps. No image augmentation techniques are applied during either the adaptation or evaluation phases.

All experiments are conducted on NVIDIA V100 GPUs equipped with 32GB memory. We implement our approach using the PyTorch deep learning framework. To ensure statistical robustness and fairness in our comparisons, we repeat each experiment three times, reporting average performance along with standard deviation. We have provided detailed instructions and step-by-step scripts in [our repository](#), clearly demonstrating how to generate datasets, perform the described test-time adaptations, and reproduce our reported results.

We adapt other baseline methods (TENT [8], TPT [6], WATT [5], CLIPArTT [31]) to work with spatial tokens. General adaptation hyperparameters (optimizer, learning rate, adaptation steps, and

batch size) remain consistent with our setup. Method-specific hyperparameters or components are retained as reported in their original implementations. Specifically, for WATT, we used the sequential version (WATT-S) with default values of $l = 2$ and $m = 5$, for CLIPArTT we used the default $k = 3$, and for TPT we used the 4 learnable tokens. Adapting these baseline methods to the segmentation task allowed us to systematically evaluate how various adaptation strategies—such as prompt tuning (TPT), pseudo-labeling (WATT, CLIPArTT), prompt refinement (CLIPArTT), and weight averaging (WATT)—perform in the context of open-vocabulary segmentation.

C Template Details

Table 5 lists the seven prompt templates used in our MLMP method. These templates were selected by the original CLIP authors² and are general-purpose, not tailored to any specific image content. The CLIP repository also provides a full set of 80 prompt templates, which we use for larger-scale ablations.

More specifically, for the ablation in Fig. 4 of the main paper, we vary the number of templates T as follows:

- $T = 1$: the default CLIP prompt “a photo of a {class}”
- $T = 3$: the first three templates $\{T^1, T^2, T^3\}$ in Table 5
- $T = 7$: all seven templates $\{T^1, \dots, T^7\}$ in Table 5
- $T = 20$: the first 20 templates from the 80-template pool
- $T = 80$: the complete set of 80 CLIP templates

Table 5: List of the seven prompt templates used in our MLMP method. These general-purpose templates, originally proposed by the CLIP authors, serve as diverse textual views of each class and are not tailored to specific datasets or domains.

ID	Prompt template
T^1	itap of a {class}
T^2	a bad photo of the {class}.
T^3	a origami {class}.
T^4	a photo of the large {class}.
T^5	a {class} in a video game.
T^6	art of the {class}.
T^7	a photo of the small {class}.

D Dataset Details

This section details the datasets used in our experiments, along with the synthetic corruptions applied to evaluate robustness under distribution shifts.

More specifically, we conduct experiments on a diverse set of segmentation benchmarks:

- **Pascal VOC (V20/V21)** [34]: Contains 20 foreground object classes (v20) with a background class (v21), widely used for benchmarking semantic segmentation tasks.
- **Pascal Context (P59/P60)** [35]: An extension of the Pascal VOC 2010 dataset, providing pixel-level annotations for more than 400 classes. Due to sparsity, a frequently used subset includes 59 object classes plus a background class, totaling 60 categories.
- **Cityscapes** [36]: A large-scale dataset for semantic segmentation of urban street scenes. It comprises around 5,000 finely annotated images from 50 cities, recorded under various daylight conditions, featuring dynamic objects, varying layouts, and changing backgrounds, capturing significant natural domain shifts.

²https://github.com/openai/CLIP/blob/main/notebooks/Interacting_with_CLIP.ipynb

- **COCO-Stuff** [37]: Extends the original COCO dataset by adding annotations for background categories ("stuff"), resulting in 171 classes—80 objects, and 91 stuff categories.
- **COCO-Object** [38]: A subset of the original COCO dataset, consisting exclusively of 80 object categories without background annotations.

In addition to the original versions of each dataset—some of which already reflect natural domain shifts (e.g., Cityscapes)—we further assess the robustness of all methods by applying synthetic corruptions. Inspired by ImageNet-C [33], we apply **15 synthetic corruptions** to evaluate the robustness of segmentation models under various perturbations. These corruptions include Gaussian noise, shot noise, impulse noise, defocus blur, glass blur, motion blur, zoom blur, snow, frost, fog, brightness variations, contrast variations, elastic transformations, pixelation, and JPEG compression. Each corruption is applied at severity level 5, representing the most challenging scenario.

We resize images from all datasets to 224×224 pixels. Due to the high resolution of Cityscapes images, we process them as overlapping patches of size 224×224 pixels (with overlaps of 112 pixels). Predictions for these patches are subsequently aggregated to produce the final segmentation maps.

This curated set of 82 distinct test scenarios rigorously benchmarks our method across a comprehensive spectrum of conditions. It encompasses not only typical natural domain shifts and synthetic corruptions but also significant variations in image resolution, scene complexity, object scale, and semantic granularity.

E Computational Complexity

In this section, we provide an exhaustive analysis of each test-time adaptation method’s resource footprint by measuring: (i) latency, (ii) floating-point operations (FLOPs), (iii) peak GPU memory usage, and (iv) number of learnable parameters. For a fair comparison, all measurements were performed on a single test sample using the same NVIDIA V100 (32 GB) GPU. The results are summarized in Table 6.

We compare TENT, TPT, CLIPArTT, WATT, and our MLMP across all four complexity metrics. In TENT, WATT, CLIPArTT, and MLMP, only the LayerNorm parameters of the vision encoder are updated during adaptation, whereas TPT introduces additional learnable tokens at the input of the text encoder. Additionally TENT, WATT, and MLMP use a fixed sets of text features without a need for recalculating them during adaptation/evaluation, so all prompt templates can be encoded once (✓ in the “One-time Text Encoder” column) and then reused throughout both adaptation and evaluation phases. In contrast, TPT and CLIPArTT modify prompt embeddings or refine text templates during adaptation, requiring multiple forward passes through the text encoder.

In terms of latency, MLMP completes both adaptation and evaluation in just 0.582 ms, which is only marginally slower than TENT (0.480 ms) but substantially faster than WATT (5.215 ms) and CLIPArTT (3.525 ms). Despite leveraging multi-level fusion and multiple prompt templates, MLMP maintains a lightweight computational profile with only 82.4 GFLOPs and 82.9 GFLOPs for adaptation and evaluation, respectively—comparable to TENT and significantly lower than all other baselines. Furthermore, MLMP’s peak memory usage is among the lowest at 2,093.9 MB, and like TENT, it updates only 0.02% of the model parameters. These results highlight MLMP’s efficiency: it delivers rich representational capacity through multi-level and multi-prompt integration by boosting the results significantly (as shown in Table 4 of the main paper), yet remains almost as lightweight as the simplest baseline.

F Performance with a Single Test Sample

As shown in Table 7, while TENT yields improvements on the original dataset, it leads to a performance drop on V20-C. In contrast, our method, MLMP, consistently improves performance over the no adaptation baseline, with gains of 8.77% on the otiginal data and 9.40% on the average across corruptions.

Table 6: Computational-complexity comparison across methods. For GFLOPs, only the forward-pass cost in adaptation and evaluation is measured; by common practice, the cost of back-propagation in adaptation phase can be approximated as twice the forward cost. A ✓ in the second column indicates that all text information are encoded *once* and cached. A dagger (†) indicates that TPT adds additional parameters beyond the original network.

Method	One-time Text Encoder	Time (sec.) ↓		GFLOPs ↓		Max Memory (MB) ↓	Learn. Params (Ratio) ↓
		Adapt	Eval	Adapt	Eval		
TENT	✓	0.462	0.018	79.1	79.1	2,068.4	102,400 (0.02%)
TPT	✗	0.445	0.031	275.6	275.6	2,583.1	3,072 [†] (<0.01%)
CLIPArTT	✗	3.494	0.031	1,755.5	275.6	8,928.5	102,400 (0.02%)
WATT	✓	5.197	0.018	553.9	79.1	7,232.4	716,800 (0.17%)
MLMP (ours)	✓	0.541	0.041	82.4	82.9	2,093.9	102,400 (0.02%)

Table 7: mIoU performance comparison when using a single test sample for V20 dataset.

OVSS Backbone: NAACLIP	Adaptation Method		
	No Adapt.	TENT	MLMP
Dataset: V20			
Original	75.91	76.20	84.68
Gaussian noise	62.89	62.59	71.92
Shot noise	66.26	65.45	75.78
Impulse noise	63.16	63.34	72.35
Defocus blur	72.59	71.37	80.91
Glass blur	71.44	69.95	79.29
Motion blur	73.10	72.55	81.64
Zoom blur	59.03	60.64	69.99
Snow	71.49	70.03	80.64
Frost	65.38	65.96	74.33
Fog	70.69	69.39	80.77
Brightness	74.95	74.73	84.58
Contrast	71.51	69.74	79.78
Elastic transform	62.86	65.09	75.32
Pixelate	77.28	75.84	85.63
JPEG compression	72.59	70.85	83.20
V20-C Average	69.01	68.50	78.41

G Generalization Across Model Variants

To evaluate the robustness and generality of our method, we conduct a series of experiments using different model configurations within the segmentation pipeline. Specifically, we assess how MLMP performs when (i) changing the vision transformer backbone, (ii) switching between different open-vocabulary semantic segmentation (OVSS) formulations, and (iii) adopting an entirely different vision–language model. These experiments demonstrate that our method maintains consistent improvements across a wide range of architectural and algorithmic configurations, confirming its flexibility and transferability.

G.1 Comparison Across ViT Backbones

To evaluate whether our method generalizes across different vision transformer backbones, we replicate the main experiments using ViT-B/16 and ViT-B/32 in place of the default ViT-L/14 model. These backbones represent lighter configurations, with fewer parameters and larger patch (32 and 16). As shown in Tables 8 and 9, MLMP continues to provide substantial improvements over all baselines across both configurations, on both clean data (V20 Original) and under severe synthetic corruptions. These results confirm that the benefits of our multi-level and multi-prompt adaptation strategy are not tied to model scale or specific architectural configurations, and remain effective even in lower-resolution settings.

Table 8: Performance comparison of test-time adaptation methods using the ViT-B/16 backbone with NaCLIP as the OVSS model. Results are reported as mIoU scores on the V20 dataset (original) and 15 corruption types. MLMP achieves the highest performance across all settings, demonstrating strong robustness even with a smaller backbone.

OVSS Backbone: NaCLIP		Adaptation Method					
Dataset: V20		No Adapt.	TENT	TPT	WATT	CLIPArTT	MLMP
Original		77.62	79.15 \pm 0.06	77.63 \pm 0.01	43.18 \pm 0.07	72.70 \pm 0.17	84.18 \pm 0.07
Gaussian noise		48.00	52.04 \pm 0.12	48.11 \pm 0.00	18.83 \pm 0.14	33.80 \pm 0.52	61.67 \pm 0.00
Shot noise		52.49	55.56 \pm 0.16	52.41 \pm 0.00	19.86 \pm 0.12	37.62 \pm 0.33	64.97 \pm 0.10
Impulse noise		49.51	52.87 \pm 0.11	49.41 \pm 0.01	19.12 \pm 0.23	35.92 \pm 0.05	61.15 \pm 0.09
Defocus blur		68.03	69.85 \pm 0.04	67.88 \pm 0.01	37.54 \pm 0.17	56.77 \pm 0.19	76.71 \pm 0.02
Glass blur		62.17	65.14 \pm 0.17	62.45 \pm 0.00	31.12 \pm 0.08	47.86 \pm 0.15	72.62 \pm 0.04
Motion blur		69.56	71.93 \pm 0.02	69.54 \pm 0.01	36.89 \pm 0.15	58.64 \pm 0.29	77.08 \pm 0.03
Zoom blur		47.34	52.30 \pm 0.19	47.38 \pm 0.01	22.83 \pm 0.12	33.52 \pm 0.20	59.05 \pm 0.20
Snow		60.88	64.38 \pm 0.05	61.24 \pm 0.00	27.68 \pm 0.21	49.91 \pm 0.38	71.41 \pm 0.15
Frost		55.45	58.38 \pm 0.14	55.44 \pm 0.00	29.66 \pm 0.23	46.94 \pm 0.04	67.42 \pm 0.09
Fog		67.07	70.01 \pm 0.02	67.07 \pm 0.00	35.84 \pm 0.23	59.98 \pm 0.09	76.32 \pm 0.02
Brightness		73.33	75.14 \pm 0.17	73.23 \pm 0.00	40.87 \pm 0.09	67.30 \pm 0.33	82.14 \pm 0.03
Contrast		60.30	63.30 \pm 0.04	60.20 \pm 0.00	29.68 \pm 0.12	48.42 \pm 0.55	70.02 \pm 0.04
Elastic transform		50.14	54.83 \pm 0.01	50.00 \pm 0.01	23.32 \pm 0.14	43.67 \pm 0.00	63.65 \pm 0.07
Pixelate		75.48	77.44 \pm 0.03	75.31 \pm 0.01	42.26 \pm 0.08	67.33 \pm 0.08	83.29 \pm 0.01
JPEG compression		69.17	70.97 \pm 0.07	69.15 \pm 0.01	34.94 \pm 0.07	60.30 \pm 0.54	79.35 \pm 0.12
V20-C Average		60.59	63.61	60.59	30.03	49.87	71.12

Table 9: Performance comparison of test-time adaptation methods using the ViT-B/32 backbone with NaCLIP as the OVSS model. Results are reported as mIoU scores on the V20 dataset (original) and 15 corruption types. MLMP achieves the highest performance across all settings, demonstrating strong robustness even with a smaller backbone and smaller patch size.

OVSS Backbone: NaCLIP		Adaptation Method					
Dataset: V20		No Adapt.	TENT	TPT	WATT	CLIPArTT	MLMP
Original		72.43	72.83 \pm 0.01	72.52 \pm 0.00	50.71 \pm 0.10	67.67 \pm 0.15	79.95 \pm 0.01
Gaussian noise		47.59	49.30 \pm 0.18	47.43 \pm 0.00	29.26 \pm 0.09	37.36 \pm 0.17	59.27 \pm 0.16
Shot noise		51.80	54.43 \pm 0.21	51.83 \pm 0.00	31.82 \pm 0.15	41.07 \pm 0.21	63.73 \pm 0.12
Impulse noise		48.79	51.59 \pm 0.11	48.79 \pm 0.00	30.31 \pm 0.04	37.65 \pm 0.17	58.81 \pm 0.04
Defocus blur		60.23	61.86 \pm 0.07	60.17 \pm 0.00	36.54 \pm 0.20	48.97 \pm 0.21	66.70 \pm 0.08
Glass blur		54.59	56.73 \pm 0.09	54.80 \pm 0.00	28.70 \pm 0.10	37.96 \pm 0.26	65.34 \pm 0.03
Motion blur		59.53	60.49 \pm 0.02	59.65 \pm 0.00	35.80 \pm 0.06	47.61 \pm 0.52	66.71 \pm 0.08
Zoom blur		38.66	41.07 \pm 0.10	38.62 \pm 0.00	21.72 \pm 0.14	24.39 \pm 0.18	49.53 \pm 0.08
Snow		49.17	51.01 \pm 0.08	48.88 \pm 0.01	27.55 \pm 0.17	40.30 \pm 0.00	62.30 \pm 0.09
Frost		47.60	50.18 \pm 0.09	47.53 \pm 0.00	28.48 \pm 0.15	39.23 \pm 0.12	60.22 \pm 0.07
Fog		56.25	59.47 \pm 0.08	56.22 \pm 0.00	35.76 \pm 0.09	47.63 \pm 0.29	68.18 \pm 0.04
Brightness		68.03	68.94 \pm 0.04	67.95 \pm 0.00	46.11 \pm 0.02	61.07 \pm 0.25	76.90 \pm 0.09
Contrast		48.79	50.67 \pm 0.07	48.88 \pm 0.02	29.54 \pm 0.06	36.64 \pm 0.05	58.81 \pm 0.11
Elastic transform		52.73	55.59 \pm 0.20	52.75 \pm 0.00	29.86 \pm 0.21	44.84 \pm 0.18	65.39 \pm 0.09
Pixelate		68.61	69.15 \pm 0.01	68.65 \pm 0.01	44.57 \pm 0.17	60.30 \pm 0.41	77.28 \pm 0.04
JPEG compression		63.86	65.12 \pm 0.05	63.87 \pm 0.00	42.85 \pm 0.11	55.44 \pm 0.08	74.40 \pm 0.09
V20-C Average		54.42	56.37	54.40	33.26	44.03	64.97

G.2 Comparison Across OVSS Methods

Our method is designed to be flexible and agnostic to the underlying open-vocabulary semantic segmentation (OVSS) formulation. While all main experiments in the paper use NaCLIP as the OVSS baseline—paired with No Adapt., TENT, TPT, CLIPArTT, WATT, and our MLMP—we further evaluate the generality of our approach by applying MLMP to two alternative OVSS methods.

Specifically, we consider the original CLIP [1], adapted for pixel-wise segmentation via patch-level similarity, and SCLIP [27], which incorporates spatial priors into the vision-language matching process. As shown in Table 10, applying MLMP on top of these OVSS baselines yields consistent improvements across both clean and corrupted settings.

Table 10: Performance comparison of test-time adaptation methods using the original CLIP [1] and SCLIP [27] as the OVSS model with a ViT-B/16 backbone. MLMP consistently improves performance across all settings, highlighting its strong generalization capabilities.

OVSS: CLIP [1]		Adaptation Method			OVSS: SCLIP [27]		Adaptation Method		
Dataset: V20		No Adapt.	TENT	MLMP	Dataset: V20		No Adapt.	TENT	MLMP
Original		33.11	51.36 ± 0.03	61.47 ± 0.01	Original		78.20	79.12 ± 0.05	84.91 ± 0.01
Gaussian noise		22.74	37.78 ± 0.11	49.35 ± 0.02	Gaussian noise		45.65	49.72 ± 0.07	61.20 ± 0.09
Shot noise		23.67	38.86 ± 0.20	50.81 ± 0.05	Shot noise		50.21	54.09 ± 0.15	64.06 ± 0.09
Impulse noise		22.36	36.63 ± 0.15	47.81 ± 0.17	Impulse noise		47.05	50.62 ± 0.05	59.73 ± 0.14
Defocus blur		31.83	48.33 ± 0.13	58.25 ± 0.04	Defocus blur		66.40	66.44 ± 0.05	75.03 ± 0.07
Glass blur		28.60	46.59 ± 0.29	56.02 ± 0.02	Glass blur		62.01	64.79 ± 0.22	72.22 ± 0.27
Motion blur		32.62	50.61 ± 0.07	59.55 ± 0.31	Motion blur		68.95	70.81 ± 0.02	76.23 ± 0.10
Zoom blur		23.42	39.43 ± 0.06	47.65 ± 0.10	Zoom blur		45.12	48.50 ± 0.11	57.84 ± 0.16
Snow		28.38	48.05 ± 0.04	55.89 ± 0.04	Snow		60.61	64.60 ± 0.20	71.70 ± 0.06
Frost		26.20	45.33 ± 0.04	53.56 ± 0.17	Frost		56.14	58.43 ± 0.03	68.57 ± 0.02
Fog		28.66	46.98 ± 0.05	56.62 ± 0.02	Fog		68.34	70.03 ± 0.17	76.57 ± 0.06
Brightness		33.71	51.77 ± 0.24	60.96 ± 0.08	Brightness		74.03	74.62 ± 0.11	82.91 ± 0.04
Contrast		26.06	42.86 ± 0.08	53.55 ± 0.04	Contrast		58.98	61.69 ± 0.08	69.57 ± 0.10
Elastic transform		27.12	45.92 ± 0.11	51.02 ± 0.21	Elastic transform		52.29	56.45 ± 0.02	65.05 ± 0.14
Pixelate		33.32	51.11 ± 0.00	61.22 ± 0.09	Pixelate		75.56	76.66 ± 0.09	82.99 ± 0.00
JPEG compression		31.64	49.76 ± 0.04	59.79 ± 0.06	JPEG compression		68.38	69.85 ± 0.12	78.69 ± 0.17
V21-C Average		28.02	45.33	54.80	V21-C Average		59.98	62.49	70.82

G.3 Generalization to Emerging VLMs

To further assess the generality of our approach, we evaluate MLMP on SigLIP v2 [39], one of the most recently introduced vision–language models. As shown in Table 11, MLMP continues to deliver consistent improvements across both natural and corrupted datasets, indicating that the core components of our method—multi-level and multi-prompt aggregation—generalize well beyond CLIP-based architectures.

Table 11: Performance comparison of test-time adaptation using SigLIP-2 as the OVSS model. Results are reported as mIoU scores on the V20 dataset. MLMP shows improvement over the baseline in most corruption types.

OVSS Backbone: SigLIP-2		Adaptation Method	
Dataset: V20		No Adapt.	MLMP
Original		66.62	67.88 ± 0.32
Gaussian noise		39.74	41.05 ± 0.34
Shot noise		40.24	43.56 ± 0.07
Impulse noise		40.76	42.43 ± 0.22
Defocus blur		47.15	50.41 ± 0.02
Glass blur		38.64	40.60 ± 0.55
Motion blur		42.30	42.98 ± 0.39
Zoom blur		27.29	29.20 ± 0.03
Snow		3.85	4.84 ± 0.03
Frost		21.32	23.12 ± 0.02
Fog		70.73	70.86 ± 0.04
Brightness		18.45	19.14 ± 0.27
Contrast		70.88	70.35 ± 0.06
Elastic transform		38.41	38.71 ± 0.05
Pixelate		57.85	59.14 ± 0.07
JPEG compression		56.35	58.55 ± 0.04
V20-C Average		40.93	42.33

H Visualization of Layer-Wise Confidence Weights

In the main paper (Fig. 3), we presented the layer-wise confidence weights for the V20, Cityscapes, and COCO-Stuff datasets. Here, we extend the analysis by visualizing the weights for four additional

datasets: V21, P59, P60, and COCO-Object in Fig. 5. As with the earlier results, we plot the mean and standard deviation of the learned weights across layers under various corruption types.

The observed trends closely mirror those reported in the main paper. In particular, deeper layers consistently receive higher confidence scores, while lower and mid-level layers still contribute under corrupted conditions. This reweighting behavior reflects the adaptive nature of our fusion strategy, which dynamically emphasizes the most reliable representations depending on the dataset and corruption type. These results further support the robustness and generality of our layer-wise uncertainty-aware fusion mechanism across diverse segmentation benchmarks.

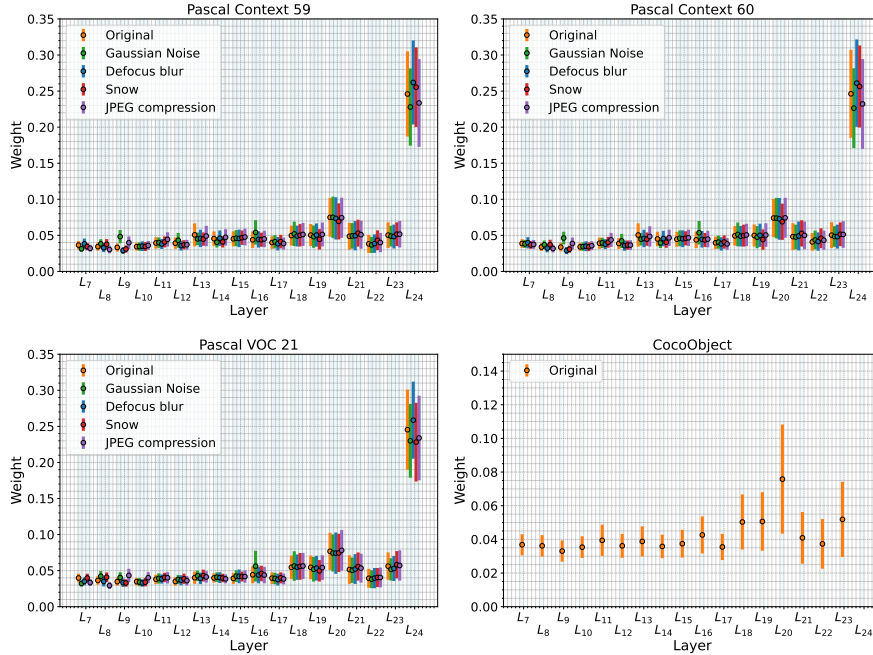


Figure 5: Mean and standard deviation of weights of intermediate layers for several datasets.

I Visualization of Segmentation Maps

Figure 6 presents qualitative segmentation results on the v20 dataset, comparing predictions from the non-adaptive baseline, TENT, and our MLMP method. MLMP demonstrates stronger spatial consistency and fewer semantic errors, particularly in challenging regions where both the baseline and TENT struggle. The integration of intermediate-layer supervision appears especially beneficial for refining small object boundaries and correcting fine-grained details.

In Figures 7–15, we provide additional qualitative examples across a range of corruption types, using NaCLIP as the our OVSS backbone. These include both successful and failure cases under Gaussian noise, defocus blur, snow, and JPEG compression. Overall, the results illustrate the robustness of MLMP in mitigating noise-induced artifacts and improving prediction confidence, while also highlighting failure modes that warrant further investigation.

J Detailed Results of the Main Paper

This section provides complete versions of the experimental results that were summarized or partially reported in the main paper. It includes full tables for ablation studies and detailed comparisons with baseline adaptation methods across various datasets and evaluation settings. These results offer a more comprehensive view of the effectiveness and robustness of our proposed approach.

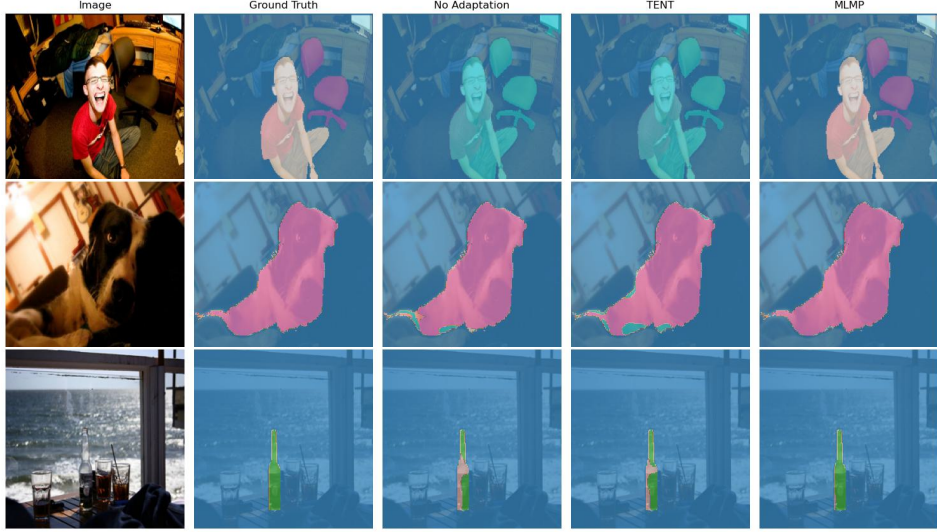


Figure 6: Qualitative results for No Adapt., TENT and MLMP on V20 Original.

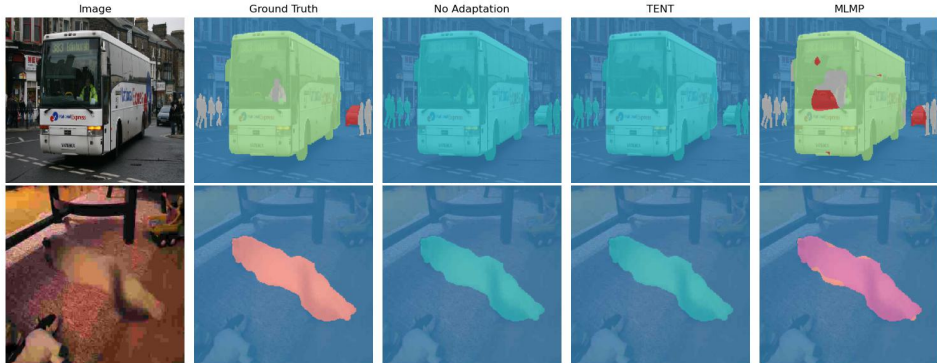


Figure 7: Failed Cases of MLMP on V20 Original.

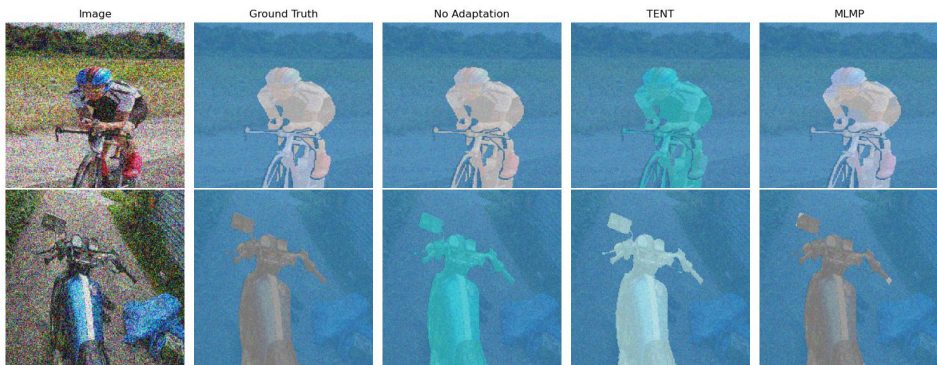


Figure 8: Good Cases of MLMP on V20 for V20 gaussian noise corruption.

J.1 Ablation Studies

We provide here the detailed versions of the tables referenced in the ablation section of the main paper. Table 12 shows the detailed results of using different layer ranges in the proposed multi-level adaptation. Table 13 reports results for different strategies to integrate different prompt templates. Table 14 presents a detailed analysis of the impact of the number of templates. Finally, Table 15

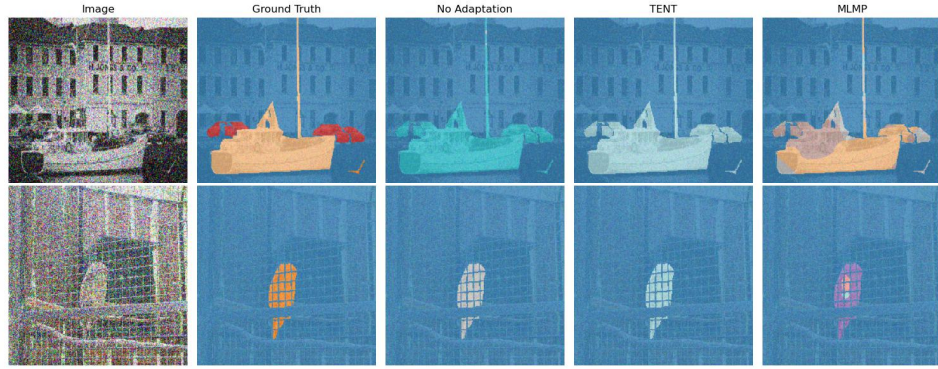


Figure 9: Failed Cases of MLMP on V20 gaussian noise corruption.

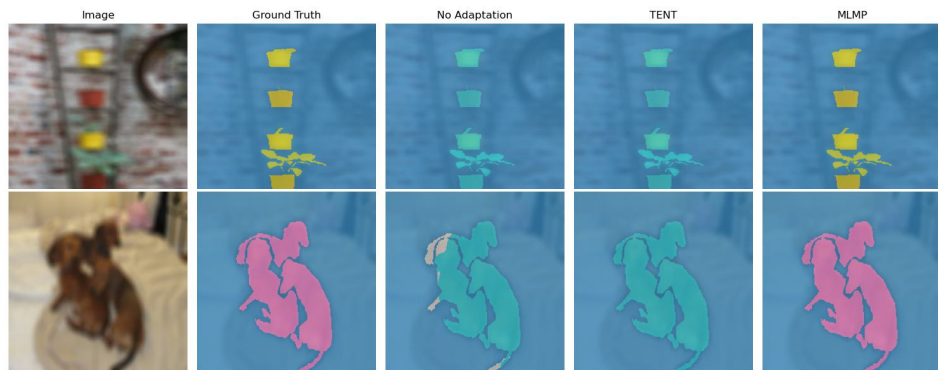


Figure 10: Good Cases of MLMP on V20 defocus blur corruption.

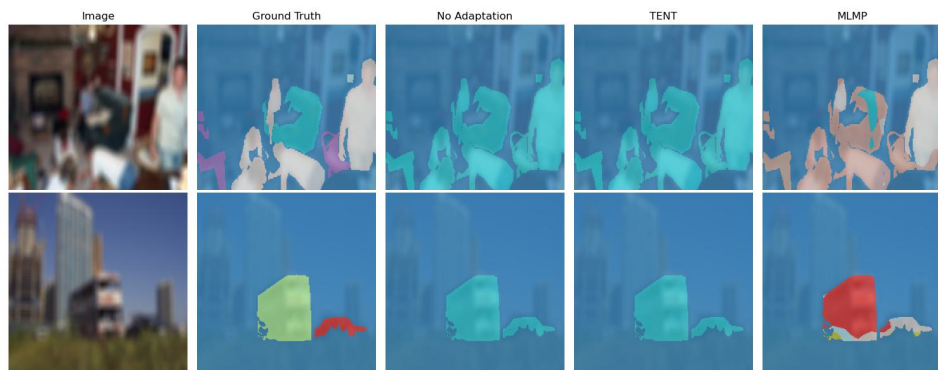


Figure 11: Failed Cases of MLMP on V20 defocus blur corruption.

presents results for the combination of all proposed components, showing individual and combined contributions.

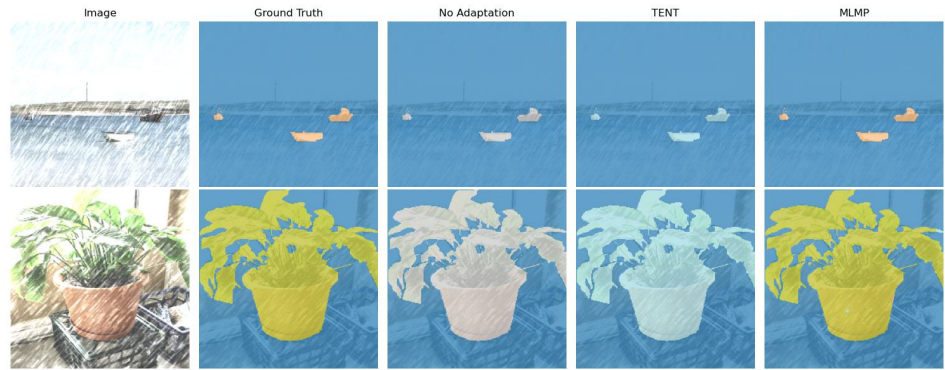


Figure 12: Good Cases of MLMP on V20 snow corruption.

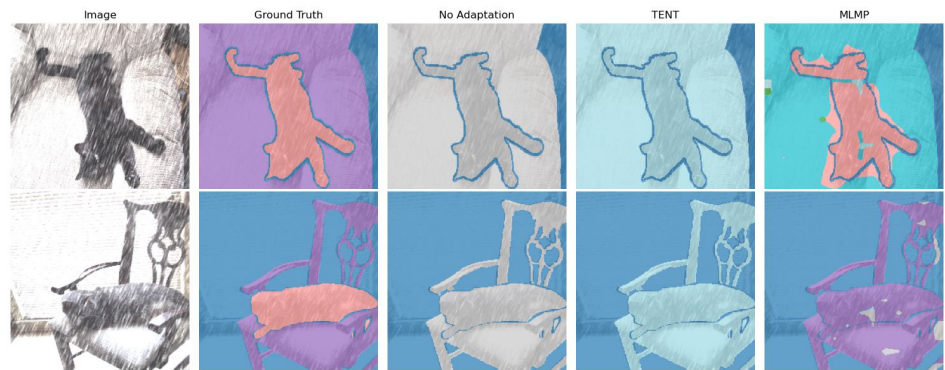


Figure 13: Failed Cases of MLMP on V20 snow corruption.



Figure 14: Good Cases of MLMP on V20 JPEG compression corruption.

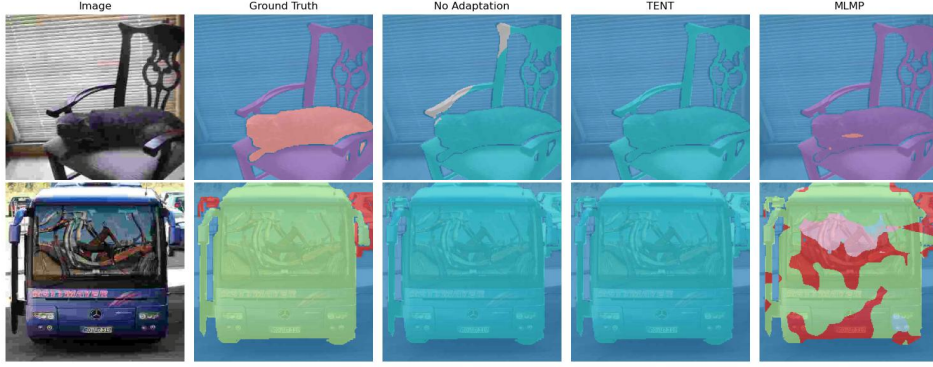


Figure 15: Failed Cases of MLMP on V20 JPEG compression corruption.

Table 12: mIoU performance over different layer aggregation strategies. Maximum value in each row is highlighted.

ViT-L/14 Layer Range	L_{24} (last)	L_{23-24} (last two)	L_{22-24} (last three)	L_{19-24} (last 25%)	L_{13-24} (last 50%)	L_{7-24} (last 75%)	L_{1-24} (all layers)
Original (V20)	77.00 ± 0.04	77.65 ± 0.02	77.66 ± 0.09	80.61 ± 0.05	80.50 ± 0.03	81.67 ± 0.04	78.79 ± 0.02
Gaussian noise	63.02 ± 0.06	64.41 ± 0.05	65.39 ± 0.13	66.88 ± 0.18	66.88 ± 0.02	67.82 ± 0.01	63.06 ± 0.09
Shot noise	65.88 ± 0.06	67.74 ± 0.11	68.43 ± 0.04	70.11 ± 0.09	70.40 ± 0.02	70.52 ± 0.12	64.88 ± 0.02
Impulse noise	64.17 ± 0.04	65.53 ± 0.09	66.19 ± 0.12	67.24 ± 0.17	67.15 ± 0.09	68.10 ± 0.01	62.09 ± 0.05
Defocus blur	72.06 ± 0.12	72.93 ± 0.19	72.84 ± 0.02	76.10 ± 0.16	76.37 ± 0.05	78.78 ± 0.02	77.56 ± 0.09
Glass blur	70.74 ± 0.07	71.73 ± 0.06	72.53 ± 0.15	74.20 ± 0.12	75.53 ± 0.05	77.66 ± 0.05	75.85 ± 0.02
Motion blur	73.50 ± 0.10	73.74 ± 0.08	74.62 ± 0.09	76.83 ± 0.07	77.50 ± 0.07	79.39 ± 0.16	77.22 ± 0.15
Zoom blur	61.36 ± 0.07	62.10 ± 0.01	62.56 ± 0.00	63.99 ± 0.20	64.59 ± 0.14	66.50 ± 0.16	64.79 ± 0.01
Snow	71.04 ± 0.05	72.09 ± 0.04	72.56 ± 0.02	74.47 ± 0.12	74.41 ± 0.01	76.39 ± 0.02	73.72 ± 0.07
Frost	67.01 ± 0.02	66.92 ± 0.02	67.23 ± 0.04	68.94 ± 0.01	70.03 ± 0.01	71.17 ± 0.00	68.23 ± 0.02
Fog	70.54 ± 0.07	71.44 ± 0.07	71.50 ± 0.05	74.50 ± 0.16	74.62 ± 0.08	76.55 ± 0.06	74.37 ± 0.03
Brightness	75.61 ± 0.02	76.27 ± 0.00	76.80 ± 0.04	79.16 ± 0.07	79.64 ± 0.16	81.34 ± 0.04	79.11 ± 0.05
Contrast	70.51 ± 0.04	71.72 ± 0.13	72.17 ± 0.00	74.58 ± 0.08	75.42 ± 0.09	76.87 ± 0.06	74.09 ± 0.00
Elastic transform	65.78 ± 0.05	66.08 ± 0.08	66.06 ± 0.06	68.62 ± 0.15	70.38 ± 0.09	70.59 ± 0.14	67.91 ± 0.12
Pixelate	76.95 ± 0.12	78.38 ± 0.02	78.46 ± 0.05	80.70 ± 0.05	81.11 ± 0.03	83.02 ± 0.04	81.53 ± 0.02
JPEG compression	71.84 ± 0.15	73.88 ± 0.11	74.40 ± 0.07	76.96 ± 0.02	77.67 ± 0.03	78.73 ± 0.08	75.87 ± 0.19
V20-C Average	69.33	70.33	70.78	72.89	73.45	74.90	72.02

Table 13: mIoU performance comparison for different strategies to integrate different prompt templates.

Dataset: V20	Text	Params	Loss
Original	78.91 ± 0.07	74.46 ± 0.21	79.70 ± 0.06
Gaussian noise	66.27 ± 0.00	62.83 ± 0.04	66.75 ± 0.01
Shot noise	69.78 ± 0.10	67.10 ± 0.12	70.03 ± 0.04
Impulse noise	66.73 ± 0.03	64.57 ± 0.52	67.88 ± 0.07
Defocus blur	74.05 ± 0.10	70.28 ± 0.16	74.31 ± 0.09
Glass blur	73.31 ± 0.08	70.28 ± 0.34	74.38 ± 0.36
Motion blur	75.20 ± 0.09	71.56 ± 0.09	75.72 ± 0.04
Zoom blur	63.31 ± 0.11	61.29 ± 0.09	64.61 ± 0.01
Snow	73.78 ± 0.02	70.10 ± 0.30	74.66 ± 0.01
Frost	68.90 ± 0.06	66.42 ± 0.04	69.50 ± 0.01
Fog	72.60 ± 0.03	67.63 ± 0.07	73.33 ± 0.03
Brightness	78.16 ± 0.02	74.05 ± 0.03	78.69 ± 0.02
Contrast	73.75 ± 0.06	69.47 ± 0.24	74.09 ± 0.01
Elastic transform	68.41 ± 0.02	64.98 ± 0.09	69.14 ± 0.05
Pixelate	79.59 ± 0.06	75.54 ± 0.05	80.09 ± 0.03
JPEG compression	74.98 ± 0.05	70.55 ± 0.11	75.56 ± 0.02
V20-C Average	71.92	68.44	72.58

Table 14: IoU performance of our method for different numbers of templates.

Dataset: V20	1 Template	3 Templates	7 Templates	20 Templates	80 Templates
Original	77.00 \pm 0.04	79.48 \pm 0.08	79.70 \pm 0.06	79.17 \pm 0.01	79.25 \pm 0.02
Gaussian noise	63.02 \pm 0.06	66.51 \pm 0.10	66.75 \pm 0.01	65.94 \pm 0.09	66.02 \pm 0.02
Shot noise	65.88 \pm 0.06	70.20 \pm 0.03	70.03 \pm 0.04	68.59 \pm 0.01	69.00 \pm 0.01
Impulse noise	64.17 \pm 0.04	67.57 \pm 0.01	67.88 \pm 0.07	66.53 \pm 0.06	66.91 \pm 0.02
Defocus blur	72.06 \pm 0.12	74.66 \pm 0.02	74.31 \pm 0.09	73.89 \pm 0.12	74.09 \pm 0.06
Glass blur	70.74 \pm 0.07	74.38 \pm 0.12	74.38 \pm 0.36	73.78 \pm 0.09	73.88 \pm 0.07
Motion blur	73.50 \pm 0.10	75.80 \pm 0.08	75.72 \pm 0.04	75.19 \pm 0.04	75.19 \pm 0.04
Zoom blur	61.36 \pm 0.07	63.47 \pm 0.02	64.61 \pm 0.01	63.50 \pm 0.03	63.84 \pm 0.04
Snow	71.04 \pm 0.05	74.09 \pm 0.08	74.66 \pm 0.01	73.78 \pm 0.03	73.91 \pm 0.01
Frost	67.01 \pm 0.02	69.09 \pm 0.01	69.50 \pm 0.01	69.08 \pm 0.00	69.10 \pm 0.02
Fog	70.54 \pm 0.07	73.69 \pm 0.01	73.33 \pm 0.03	72.87 \pm 0.03	72.86 \pm 0.05
Brightness	75.61 \pm 0.02	78.49 \pm 0.05	78.69 \pm 0.02	77.86 \pm 0.02	78.06 \pm 0.02
Contrast	70.51 \pm 0.04	74.01 \pm 0.22	74.09 \pm 0.01	73.48 \pm 0.04	73.56 \pm 0.09
Elastic transform	65.78 \pm 0.05	68.09 \pm 0.01	69.14 \pm 0.05	67.94 \pm 0.02	68.31 \pm 0.09
Pixelate	76.95 \pm 0.12	79.91 \pm 0.04	80.09 \pm 0.03	79.15 \pm 0.06	79.41 \pm 0.05
JPEG compression	71.84 \pm 0.15	75.00 \pm 0.05	75.56 \pm 0.02	74.45 \pm 0.09	74.75 \pm 0.01
V20-C Average	69.33	72.33	72.58	71.74	71.93

Table 15: Detailed mIoU comparison of MLMP components, showing individual and combined contributions.

Multi-Level Fusion	✓	✓	✓	✗	✗	✓	✓	✓	✗	✓	✓	✓
Multi-Prompt Loss	✗	✗	✗	✓	✗	✓	✓	✗	✗	✓	✓	✓
Image-Level Entropy	✗	✗	✗	✗	✓	✗	✗	✓	✓	✓	✓	✓
Uncertainty-Aware Weight.	✗	✗	✓	✗	✗	✗	✓	✓	✗	✗	✗	✓
Original	77.00 \pm 0.04	77.38 \pm 0.01	81.67 \pm 0.04	79.70 \pm 0.06	78.74 \pm 0.08	78.97 \pm 0.08	83.00 \pm 0.03	77.69 \pm 0.01	82.70 \pm 0.01	81.15 \pm 0.02	79.13 \pm 0.00	83.76 \pm 0.00
Gaussian noise	63.02 \pm 0.06	65.42 \pm 0.08	67.82 \pm 0.01	66.75 \pm 0.01	65.66 \pm 0.04	65.96 \pm 0.08	69.13 \pm 0.07	66.17 \pm 0.04	69.00 \pm 0.05	69.62 \pm 0.01	67.35 \pm 0.09	71.13 \pm 0.09
Shot noise	65.88 \pm 0.06	67.49 \pm 0.01	70.52 \pm 0.12	70.03 \pm 0.04	68.97 \pm 0.03	69.05 \pm 0.08	72.31 \pm 0.01	69.50 \pm 0.06	73.22 \pm 0.03	72.89 \pm 0.02	71.02 \pm 0.05	75.02 \pm 0.03
Impulse noise	64.17 \pm 0.04	65.11 \pm 0.17	68.10 \pm 0.01	67.88 \pm 0.07	66.35 \pm 0.12	65.39 \pm 0.12	68.86 \pm 0.13	65.16 \pm 0.10	68.77 \pm 0.15	70.31 \pm 0.09	67.17 \pm 0.09	71.34 \pm 0.11
Defocus blur	72.06 \pm 0.12	76.65 \pm 0.23	78.78 \pm 0.02	74.31 \pm 0.09	75.00 \pm 0.07	76.46 \pm 0.15	78.78 \pm 0.10	77.29 \pm 0.10	79.78 \pm 0.05	77.14 \pm 0.05	77.79 \pm 0.19	80.36 \pm 0.06
Glass blur	70.74 \pm 0.07	75.24 \pm 0.05	77.66 \pm 0.05	74.38 \pm 0.36	73.54 \pm 0.23	75.46 \pm 0.09	77.48 \pm 0.01	75.71 \pm 0.10	78.09 \pm 0.04	76.17 \pm 0.05	76.87 \pm 0.07	78.84 \pm 0.05
Motion blur	73.50 \pm 0.10	77.16 \pm 0.13	79.39 \pm 0.16	75.72 \pm 0.04	76.09 \pm 0.09	77.72 \pm 0.09	79.97 \pm 0.04	78.81 \pm 0.03	81.49 \pm 0.02	78.25 \pm 0.05	79.00 \pm 0.07	81.41 \pm 0.05
Zoom blur	61.36 \pm 0.07	64.22 \pm 0.12	66.50 \pm 0.16	64.61 \pm 0.01	64.04 \pm 0.02	66.38 \pm 0.15	68.41 \pm 0.13	65.12 \pm 0.16	67.69 \pm 0.08	68.32 \pm 0.17	67.61 \pm 0.05	69.41 \pm 0.12
Snow	71.04 \pm 0.05	72.64 \pm 0.07	76.39 \pm 0.02	74.66 \pm 0.01	74.16 \pm 0.02	73.25 \pm 0.12	77.31 \pm 0.11	74.05 \pm 0.08	78.50 \pm 0.16	77.20 \pm 0.02	74.94 \pm 0.06	79.53 \pm 0.05
Frost	67.01 \pm 0.02	67.30 \pm 0.08	71.17 \pm 0.00	69.50 \pm 0.01	69.31 \pm 0.00	67.57 \pm 0.19	71.73 \pm 0.21	68.31 \pm 0.12	72.81 \pm 0.08	71.34 \pm 0.02	68.69 \pm 0.11	73.20 \pm 0.07
Fog	70.54 \pm 0.07	72.72 \pm 0.08	76.55 \pm 0.06	73.33 \pm 0.03	73.41 \pm 0.00	75.06 \pm 0.08	78.38 \pm 0.03	73.48 \pm 0.13	77.62 \pm 0.05	75.98 \pm 0.02	75.81 \pm 0.02	79.81 \pm 0.06
Brightness	75.61 \pm 0.02	77.23 \pm 0.07	81.34 \pm 0.04	78.69 \pm 0.02	77.34 \pm 0.01	77.69 \pm 0.02	82.00 \pm 0.00	77.20 \pm 0.05	82.16 \pm 0.03	80.63 \pm 0.08	78.27 \pm 0.06	83.51 \pm 0.01
Contrast	70.51 \pm 0.04	73.36 \pm 0.08	76.87 \pm 0.06	74.09 \pm 0.01	74.14 \pm 0.14	73.57 \pm 0.05	77.42 \pm 0.09	74.09 \pm 0.11	78.09 \pm 0.08	76.97 \pm 0.01	74.75 \pm 0.08	79.06 \pm 0.16
Elastic transform	65.78 \pm 0.05	65.39 \pm 0.12	70.59 \pm 0.14	69.14 \pm 0.05	67.92 \pm 0.06	68.76 \pm 0.04	72.96 \pm 0.02	66.78 \pm 0.03	71.80 \pm 0.02	71.53 \pm 0.03	69.77 \pm 0.07	74.03 \pm 0.01
Pixelate	76.95 \pm 0.12	79.53 \pm 0.03	83.02 \pm 0.04	80.09 \pm 0.03	79.09 \pm 0.03	80.77 \pm 0.05	83.93 \pm 0.06	79.85 \pm 0.08	83.90 \pm 0.06	81.92 \pm 0.12	81.34 \pm 0.07	84.97 \pm 0.04
JPEG compression	71.84 \pm 0.15	74.38 \pm 0.12	78.73 \pm 0.08	75.56 \pm 0.02	74.77 \pm 0.11	76.77 \pm 0.00	80.81 \pm 0.09	74.61 \pm 0.06	79.79 \pm 0.02	77.98 \pm 0.02	77.94 \pm 0.07	82.06 \pm 0.01
V20-C Average	69.33	71.59	74.90	72.58	71.99	72.66	75.97	72.41	76.18	75.08	73.89	77.58

J.2 Comparison with Alternative Adaptation Methods

This section presents comprehensive tables with the full experimental results corresponding to those summarized in the main paper. Table 16 reports detailed results for the V21 dataset, Table 17 for P59, Table 18 for P60, and Table 19 for the Cityscapes dataset.

Table 16: mIoU comparison of MLMP and baseline methods on the V21 dataset, evaluated on both the original images and 15 corruption types.

OVSS Backbone: NAACLIP	Adaptation Method					
Dataset: V21	No Adapt.	TENT	TPT	WATT	CLIPArTT	MLMP
Original	45.12	45.65 \pm 0.02	45.17 \pm 0.00	28.58 \pm 0.05	39.50 \pm 0.04	50.78 \pm 0.02
Gaussian noise	37.40	37.95 \pm 0.00	37.34 \pm 0.00	20.93 \pm 0.07	30.05 \pm 0.18	43.59 \pm 0.01
Shot noise	39.33	39.17 \pm 0.03	39.23 \pm 0.00	22.06 \pm 0.06	32.07 \pm 0.17	45.55 \pm 0.02
Impulse noise	37.81	37.73 \pm 0.04	37.78 \pm 0.00	19.95 \pm 0.05	30.52 \pm 0.08	43.89 \pm 0.01
Defocus blur	41.46	41.46 \pm 0.03	41.46 \pm 0.00	24.79 \pm 0.04	34.27 \pm 0.05	46.00 \pm 0.00
Glass blur	41.76	41.55 \pm 0.01	41.82 \pm 0.00	24.61 \pm 0.03	34.55 \pm 0.16	46.83 \pm 0.04
Motion blur	42.65	42.81 \pm 0.01	42.74 \pm 0.00	25.66 \pm 0.04	36.07 \pm 0.11	47.72 \pm 0.04
Zoom blur	34.46	34.25 \pm 0.00	34.44 \pm 0.00	20.74 \pm 0.05	28.44 \pm 0.07	39.07 \pm 0.02
Snow	40.13	40.47 \pm 0.00	40.23 \pm 0.01	25.02 \pm 0.06	33.98 \pm 0.03	46.30 \pm 0.05
Frost	40.70	41.83 \pm 0.08	40.80 \pm 0.00	23.43 \pm 0.05	34.09 \pm 0.01	46.78 \pm 0.01
Fog	42.50	42.67 \pm 0.00	42.47 \pm 0.00	24.95 \pm 0.05	36.37 \pm 0.04	47.61 \pm 0.06
Brightness	44.21	44.64 \pm 0.03	44.27 \pm 0.00	27.54 \pm 0.07	38.44 \pm 0.11	49.89 \pm 0.08
Contrast	40.44	40.14 \pm 0.03	40.44 \pm 0.00	23.89 \pm 0.04	33.68 \pm 0.05	45.22 \pm 0.00
Elastic transform	40.63	41.78 \pm 0.01	40.67 \pm 0.00	24.40 \pm 0.05	35.38 \pm 0.01	46.87 \pm 0.02
Pixelate	44.70	44.95 \pm 0.03	44.79 \pm 0.00	27.74 \pm 0.06	38.14 \pm 0.06	50.11 \pm 0.01
JPEG compression	43.05	42.87 \pm 0.04	43.05 \pm 0.00	26.04 \pm 0.05	36.29 \pm 0.10	48.27 \pm 0.02
V21-C Average	40.75	40.95	40.77	24.12	34.16	46.25

Table 17: mIoU comparison of MLMP and baseline methods on the P59 dataset, evaluated on both the original images and 15 corruption types.

OVSS Backbone: NAACLIP	Adaptation Method					
Dataset: P59	No Adapt.	TENT	TPT	WATT	CLIPArTT	MLMP
Original	28.23	28.73 \pm 0.02	28.26 \pm 0.01	16.55 \pm 0.05	24.60 \pm 0.00	31.95 \pm 0.02
Gaussian noise	21.53	21.49 \pm 0.01	21.59 \pm 0.01	11.27 \pm 0.04	16.42 \pm 0.03	24.84 \pm 0.00
Shot noise	22.35	22.31 \pm 0.01	22.26 \pm 0.00	11.80 \pm 0.04	17.47 \pm 0.00	25.62 \pm 0.01
Impulse noise	21.74	21.59 \pm 0.01	21.72 \pm 0.00	11.24 \pm 0.03	17.17 \pm 0.00	24.75 \pm 0.01
Defocus blur	25.42	25.14 \pm 0.00	25.41 \pm 0.00	14.31 \pm 0.04	20.71 \pm 0.00	27.95 \pm 0.03
Glass blur	25.03	24.70 \pm 0.01	25.01 \pm 0.00	13.93 \pm 0.03	20.63 \pm 0.00	27.66 \pm 0.05
Motion blur	26.11	26.00 \pm 0.02	26.13 \pm 0.01	15.13 \pm 0.03	21.72 \pm 0.00	29.12 \pm 0.03
Zoom blur	19.20	19.49 \pm 0.03	19.20 \pm 0.00	10.86 \pm 0.03	15.39 \pm 0.00	21.98 \pm 0.02
Snow	22.45	22.29 \pm 0.02	22.45 \pm 0.00	13.60 \pm 0.04	19.17 \pm 0.01	25.47 \pm 0.01
Frost	21.95	21.94 \pm 0.00	21.97 \pm 0.00	12.83 \pm 0.03	18.77 \pm 0.04	24.52 \pm 0.01
Fog	24.85	24.91 \pm 0.03	24.86 \pm 0.00	13.85 \pm 0.05	20.66 \pm 0.00	27.84 \pm 0.01
Brightness	27.39	27.80 \pm 0.01	27.42 \pm 0.00	15.55 \pm 0.04	23.56 \pm 0.00	30.63 \pm 0.01
Contrast	23.55	23.58 \pm 0.01	23.54 \pm 0.00	13.38 \pm 0.05	19.12 \pm 0.00	26.95 \pm 0.00
Elastic transform	23.30	23.86 \pm 0.02	23.30 \pm 0.01	12.88 \pm 0.04	20.28 \pm 0.00	27.16 \pm 0.01
Pixelate	27.61	27.55 \pm 0.01	27.62 \pm 0.00	15.84 \pm 0.05	23.47 \pm 0.00	31.23 \pm 0.01
JPEG compression	25.75	25.51 \pm 0.05	25.75 \pm 0.00	14.09 \pm 0.03	21.20 \pm 0.00	29.66 \pm 0.02
P59-C Average	23.88	23.88	23.88	13.37	19.72	27.03

Table 18: mIoU comparison of MLMP and baseline methods on the P60 dataset, evaluated on both the original images and 15 corruption types.

OVSS Backbone: NAACLIP		Adaptation Method					
Dataset: P60		No Adapt.	TENT	TPT	WATT	CLIPArTT	MLMP
Original		24.95	25.29	24.98 \pm 0.01	14.77 \pm 0.04	21.88 \pm 0.01	27.99 \pm 0.03
Gaussian noise		19.31	19.17 \pm 0.01	19.34 \pm 0.01	10.29 \pm 0.03	14.91 \pm 0.01	22.22 \pm 0.02
Shot noise		19.98	19.83 \pm 0.02	19.91 \pm 0.01	10.82 \pm 0.03	15.82 \pm 0.01	22.81 \pm 0.01
Impulse noise		19.56	19.27 \pm 0.01	19.54 \pm 0.00	10.34 \pm 0.03	15.58 \pm 0.00	22.26 \pm 0.01
Defocus blur		22.74	22.38 \pm 0.01	22.72 \pm 0.01	12.79 \pm 0.04	18.67 \pm 0.00	24.92 \pm 0.01
Glass blur		22.49	22.05 \pm 0.01	22.48 \pm 0.01	12.64 \pm 0.03	18.61 \pm 0.00	24.71 \pm 0.05
Motion blur		23.28	23.01 \pm 0.03	23.30 \pm 0.01	13.53 \pm 0.03	19.51 \pm 0.01	25.71 \pm 0.03
Zoom blur		17.42	17.58 \pm 0.03	17.42 \pm 0.00	9.95 \pm 0.03	14.07 \pm 0.01	19.70 \pm 0.02
Snow		20.06	19.80 \pm 0.01	20.06 \pm 0.01	12.29 \pm 0.04	17.20 \pm 0.02	22.64 \pm 0.02
Frost		19.71	19.61 \pm 0.01	19.73 \pm 0.01	11.59 \pm 0.03	17.02 \pm 0.04	22.02 \pm 0.01
Fog		22.20	22.09 \pm 0.02	22.20 \pm 0.01	12.50 \pm 0.03	18.53 \pm 0.01	24.89 \pm 0.00
Brightness		24.35	24.56 \pm 0.01	24.37 \pm 0.01	13.87 \pm 0.04	21.05 \pm 0.01	27.02 \pm 0.00
Contrast		21.09	21.00 \pm 0.03	21.08 \pm 0.01	12.04 \pm 0.03	17.24 \pm 0.01	24.17 \pm 0.02
Elastic transform		21.17	21.46 \pm 0.01	21.19 \pm 0.01	11.70 \pm 0.04	18.53 \pm 0.01	24.27 \pm 0.02
Pixelate		24.52	24.33 \pm 0.01	24.54 \pm 0.01	14.17 \pm 0.04	21.01 \pm 0.01	27.48 \pm 0.00
JPEG compression		22.99	22.65 \pm 0.02	24.54 \pm 0.01	12.65 \pm 0.03	19.05 \pm 0.01	26.24 \pm 0.01
P60-C Average		21.39	21.25	21.49	12.08	17.79	24.07

Table 19: mIoU comparison of MLMP and baseline methods on the CityScapes dataset, evaluated on both the original images and 15 corruption types.

OVSS Backbone: NAACLIP		Adaptation Method				
Dataset: CityScapes		No Adapt.	TENT	TPT	WATT	MLMP
Original		29.49	30.54 \pm 0.04	29.57 \pm 0.01	20.77 \pm 0.02	33.35 \pm 0.03
Gaussian noise		16.14	15.00 \pm 0.02	15.94 \pm 0.01	10.19 \pm 0.01	15.32 \pm 0.00
Shot noise		20.18	19.38 \pm 0.01	20.15 \pm 0.01	12.41 \pm 0.02	20.57 \pm 0.04
Impulse noise		16.37	14.59 \pm 0.02	16.35 \pm 0.01	8.56 \pm 0.02	15.76 \pm 0.05
Defocus blur		23.34	23.50 \pm 0.02	23.46 \pm 0.01	15.63 \pm 0.02	24.86 \pm 0.08
Glass blur		24.41	24.04 \pm 0.04	24.29 \pm 0.00	15.44 \pm 0.01	25.70 \pm 0.02
Motion blur		24.73	24.98 \pm 0.00	24.91 \pm 0.01	14.21 \pm 0.03	26.02 \pm 0.01
Zoom blur		14.08	14.57 \pm 0.06	14.08 \pm 0.01	5.85 \pm 0.02	14.04 \pm 0.04
Snow		19.88	20.14 \pm 0.01	19.90 \pm 0.01	9.27 \pm 0.03	22.23 \pm 0.03
Frost		16.78	16.47 \pm 0.02	16.78 \pm 0.01	10.69 \pm 0.01	17.12 \pm 0.07
Fog		22.47	22.87 \pm 0.05	22.25 \pm 0.01	14.24 \pm 0.01	23.98 \pm 0.03
Brightness		28.45	29.30 \pm 0.01	28.47 \pm 0.01	19.99 \pm 0.02	31.88 \pm 0.04
Contrast		16.10	16.35 \pm 0.03	16.07 \pm 0.01	11.05 \pm 0.01	17.04 \pm 0.00
Elastic transform		29.14	30.16 \pm 0.02	29.02 \pm 0.01	19.99 \pm 0.03	32.86 \pm 0.00
Pixelate		28.67	29.59 \pm 0.01	28.69 \pm 0.01	18.30 \pm 0.01	32.72 \pm 0.04
JPEG compression		23.69	23.62 \pm 0.01	23.67 \pm 0.01	15.98 \pm 0.02	25.26 \pm 0.03
CityScapes-C Average		21.63	21.64	21.60	13.45	23.02